The role of trapped fluids during the development and deformation of a carbonate/shale intra-wedge tectonic mélange (Mt. Massico, Southern Apennines, Italy)

Published Version:
Smeraglia L., Aldega L., Bernasconi S.M., Billi A., Boschi C., Caracausi A., et al. (2020). The role of trapped fluids during the development and deformation of a carbonate/shale intra-wedge tectonic mélange (Mt. Massico, Southern Apennines, Italy). JOURNAL OF STRUCTURAL GEOLOGY, 138, --- [10.1016/j.jsg.2020.104086].

Availability:
This version is available at: https://hdl.handle.net/11585/770627 since: 2020-09-08

Published:
DOI: http://doi.org/10.1016/j.jsg.2020.104086

(Article begins on next page)

Smeraglia L.; Aldega L.; Bernasconi S.M.; Billi A.; Boschi C.; Caracausi A.; Carminati E.; Franchini S.; Rizzo A.L.; Rossetti F.; Vignaroli G.: *The role of trapped fluids during the development and deformation of a carbonate/shale intra-wedge tectonic mélange (Mt. Massico, Southern Apennines, Italy)*

JOURNAL OF STRUCTURAL GEOLOGY
VOL. 138
ISSN 0191-8141
DOI: 10.1016/j.jsg.2020.104086

The role of trapped fluids during the development and deformation of a carbonate/shale intra-wedge tectonic mélange

Luca Smeraglia[1,2,3*], Luca Aldega[4], Stefano Bernasconi[5] Andrea Billi[1], Chiara Boschi[6], Antonio Caracausi[7], Eugenio Carminati[1,4], Stefania Franchini[1,4], Andrea Luca Rizzo[7], Federico Rossetti[8], Gianluca Vignaroli[9]

1. Consiglio Nazionale delle Ricerche, IGAG, c.o. Dipartimento di Scienze della Terra, Sapienza Università di Roma, P.le Aldo Moro 5, 00185 Roma, Italy
2. formerly at Dipartimento di Scienze della Terra, Sapienza Università di Roma, P.le Aldo Moro 5, 00185, Roma, Italy
3. formerly at Chrono-Environnement, Université de Bourgogne Franche-Comté, 16 Route de Gray, 25000 Besançon, France.
4. Dipartimento di Scienze della Terra, Sapienza Università di Roma, P.le Aldo Moro 5, 00185, Roma, Italy
5. Geological Institute, ETH Zürich, Sonneggstrasse 5, 8092 Zürich, Switzerland
6. Istituto di Geoscienze e Georisorse, Consiglio Nazionale delle Ricerche, Via Moruzzi 1, 56124 Pisa, Italy
7. Istituto Nazionale di Geofisica e Vulcanologia, Sezione di Palermo, Via Ugo La Malfa 153, 90146 Palermo, Italy
8. Dipartimento di Scienze, Università Roma Tre, Largo San Leonardo Murialdo, 1, 00146, Roma, Italy
9. Dipartimento di Scienze Biologiche, Geologiche e Ambientali, BiGeA, Università di Bologna, 40126 Bologna, Italy

Luca Smeraglia: luca.smeraglia@cnr.it

Luca Aldega: luca.aldega@uniroma1.it

Stefano Bernasconi: stefano.bernasconi@erdw.ethz.ch

Andrea Billi: andrea.billi@cnr.it

Chiara Boschi: chiara.boschi@igg.cnr.it

Antonio Caracausi: antonio.caracausi@ingv.it

Eugenio Carminati: eugenio.carminati@uniroma1.it

Stefania Fanchini: stefania.franchini@uniroma1.it

Andrea Luca Rizzo: andrea.rizzo@ingv.it

Federico Rossetti: federico.rossetti@uniroma3.it

Gianluca Vignaroli: gianluca.vignaroli@unibo.it

*Corresponding author: Dipartimento di Scienze della Terra, Sapienza Università di Roma, Piazzale Aldo Moro 5, 00185 Roma, Italy. Phone +39 06 49914156

E-mail address: luca.smeraglia@cnr.it (Luca Smeraglia)

Abstract: In contrast to the numerous studies on exhumed tectonic mélanges along subduction channels, in accretionary wedge interiors, deformation mechanisms and related fluid circulation in tectonic mélanges are still underexplored. Here we combine structural and microstructural observations with geochemical (stable and clumped isotopes and isotope composition of noble gases in fluid inclusions of calcite veins) and geochronological data (U-Pb dating) to define deformation mechanisms and syn-tectonic fluid circulation within the Mt. Massico intra-wedge tectonic mélange, located in the inner part of the central-southern Apennines accretionary wedge, Italy. This mélange developed at the base of a clastic succession, and shear deformation was characterized by disruption of the primary bedding, mixing, and deformation of relicts of competent olistoliths and strata within a weak matrix of deformed clayey and marly interbeds. Recurrent cycles of mutually overprinting fracturing/veining and pressure-solution processes generated a block-in-matrix texture. The geochemical signatures of syn-tectonic calcite veins suggest calcite precipitation in a closed system from warm (108-147 °C) paleofluids, with $\delta^{18}O$ composition between +9‰ and 14‰, such as trapped pore water from diagenesis after extensive ^{18}O exchange with the local limestone host rock ($\delta^{18}O$ values between +26‰ and +30‰) and/or derived by clay dehydration processes (at T > 120 °C). The $^{3}He/^{4}He$ ratios in fluid inclusions trapped in calcite veins are lower than 0.1 Ra, hence He was exclusively sourced from the crust, excluding mantle-derived fluids. We conclude that: (1) intraformational rheological contrasts, inherited trapped fluids, and low-permeability barriers such as clay-rich stylolites, can favour the development of fluid overpressure and the generation of intra-wedge tectonic mélanges; (2) clay-rich intra-wedge tectonic mélanges may generate efficient barriers within accretionary wedges for vertical and lateral redistribution of fluids from reservoirs outside the mélange. We highlight that the integration of geochemical and geochronological methods can be a powerful approach to better constrain, in the future, the burial-thermal evolution of fold and thrust belts and sedimentary basins.

Keywords: tectonic mélange; fault-fluid interaction; stable and clumped isotopes; carbonates and shales; fold and thrust belt

1. Introduction

Décollements and thrust faults are major structures that control the internal architecture of fold-and-thrust belts (e.g. Morley et al., 2017). In particular, décollements commonly generate along evaporite- or clay-rich formations, control the style and timing of folding and tectonic imbrication, and may act as barriers or conduits for crustal flow of fluids, including hydrocarbons. Décollements can often act as channelized paths for fluid redistribution within the crust (e.g. Vrolijk et al., 1988; Vannucchi et al., 2008).

The shearing of clay-rich and initially layered formations along décollements can generate tectonic mélanges through primary bedding disruption, pressure-solution, veining, and offscraping/mixing of blocks from competent formations located above and below the décollement horizon (see Festa et al., 2012 for review). Such deformations can lead to block-in-matrix fabrics, consisting of competent blocks scattered in a weak matrix, which are typically characterized by heterogeneous mechanical and permeability properties (e.g. Fagereng, 2011). Outcrop, microstructural, and geochemical characterizations of tectonic mélanges can contribute to constrain their spatio-temporal evolution as well as the mechanical properties and hydrogeological characteristics (paleofluid flow).

In this context, several studies focused on tectonic mélanges exhumed from basal décollements at the subduction interface along the toe of accretionary wedges and from subduction channels (e.g. Meneghini et al., 2009; Vannucchi et al., 2008; see Festa et al., 2012 for review), where deformation can reach metamorphic conditions (e.g. Fagereng and Cooper, 2010). Only few studies focused on intra-wedge tectonic mélanges developed at diagenetic P-T conditions along décollements at the base of thrust sheets (e.g. Vannucchi and Bettelli, 2002; Codegone et al., 2012; Dewever et al., 2013; Ogata et al., 2012; Smeraglia et al., 2019). However, intra-wedge tectonic mélanges may strongly affect the mechanical behavior of inner décollements, thus influencing accretionary wedge geometry and kinematics, and can modulate the transport of fluids (i.e. water, hydrocarbon) across fold-and-thrust belts. Therefore, the understanding of mechanical and hydrological properties of exhumed mélanges is fundamental to unravel fluid (paleo)pathways and asses potential reservoirs for geofluid (i.e. hydrocarbon) accumulation in fold-and-thrust belts.

For these reasons, here we combine outcrop and microstructural observations with geochemical analyses (stable and clumped isotopes and isotope composition of noble gases in fluid inclusions of calcite veins) to unravel the deformation mechanisms, paleohydrology (i.e., fluid conduit/barrier behavior), and the temperature conditions during fluid flow within a 150 m-thick intra-wedge tectonic mélange in the Mt. Massico Ridge (e.g. Billi et al., 1997; Vitale et al., 2018; Smeraglia et al., 2019), which is located in the inner sector (Tyrrhenian side) of the central-southern Apennines fold-and-thrust belt. In this area, outcrop conditions allowed the reconstruction of syn-tectonic paleofluid circulation and the unraveling of progressive intra-wedge mélange deformation, from the undeformed host rock to the finite fabric development by tectonic deformation.

2. Geological background

2.1 Central-southern Apennines

The central-southern Apennines are a late Oligocene to present fold-and-thrust belt generated by the eastward rollback of the west-dipping subduction of the Adriatic plate below the European continental margin (Fig. 1a; e.g., Carminati et al., 2012). Orogenic accretion was accomplished through and accommodated by a set of NE-verging thrust systems, which scraped off pre- and syn-orogenic deposits of the Adriatic plate (Fig. 1b). The pre-orogenic deposits consist of ~4,000-5,000 m-thick Upper Triassic-Middle Miocene carbonate platform deposits (i.e. Apennine platform; e.g. Vezzani et al., 2010; Vitale and Ciarcia, 2018) and of ~100 m-thick middle Miocene hemipelagic marls deposited in a transitional foreland-to-foredeep environment (e.g., Vezzani et al., 2010). The syn-orogenic deposits consist of up to ~3,100 m-thick upper Miocene siliciclastic sandstones, marls, and claystones deposited in a foredeep environment (e.g., Vitale and Ciarcia, 2018). Thrust faults developed during wedge accretion and juxtaposed pre-orogenic deposits onto syn-orogenic sediments, generating stacks of imbricate thrust sheets from the surface down to depths of ~10 km (Fig. 1a,b; e.g. Mostardini and Merlini, 1986; Vezzani et al., 2010). Since early Pliocene time, the internal and axial part of the central-southern Apennines belt underwent tectonic uplift and regional extension, related to the opening of the Tyrrhenian backarc basin and accommodated by the development of NW-SE-oriented extensional faults (Fig. 1a,b; Malinverno and Ryan, 1986).

2.2 The Mt. Massico ridge

Mt. Massico is a NNE-SSW-trending ridge located in the innermost part of the central-southern Apennines (Fig. 1a; e.g. Billi et al., 1997; Luiso et al., 2018; Vitale et al., 2018). It is bounded by NE-striking active extensional faults and surrounded by the Quaternary Garigliano and Volturno river plains, the Roccamonfina volcano (Quaternary), and the Tyrrhenian Sea basin (Figs. 1a and 2a).

In the central and northeastern parts of the Mt. Massico ridge, Upper Triassic to Upper Cretaceous carbonates are exposed (Fig. 1a; Vitale et al., 2018) and arranged to form a ENE-verging asymmetric anticline with an upright forelimb and a WSW-dipping (40°-50°) backlimb (Fig. 1a). In the forelimb, a thrust juxtaposes Upper Cretaceous limestones onto Tortonian syn-orogenic sandstones (see Figure 2 in Sgrosso, 1974). The WSW-dipping backlimb continues in the southwestern part of the ridge, where middle-upper Miocene sediments are exposed (Fig. 2a,b).

This succession lies paraconformably atop Upper Cretaceous limestones and begins from the bottom with ~50 m-thick bryozoan-rich limestones of the Cusano Fm., followed upward by hemipelagic marls of the Longano Fm., with a preserved thickness of less than 1-3 meters (Sgrosso, 1974; Vitale et al., 2018) (Fig. 2a). Both these formations were deposited in a foreland environment and are Serravallian in age (Sgrosso, 1974). Above the hemipelagic marls, the sedimentary succession evolves into the Tortonian-lower Messinian siliciclastic/carbonaticlastic deposits of the

Caiazzo Fm. (hereafter called clastic deposits, Fig. 2a,b), which are interpreted as wedge-top basin deposits (Vitale et al., 2018). The clastic deposits are made up of: (1) massive-to-bedded siliciclastic sandstones with clayey, marly, and calcarenite interbeds and (2) polymictic breccias/conglomerates characterized by Mesozoic-Cenozoic carbonate blocks and siliciclastic clasts (up to a few dm^3 in volume), including also clasts of volcanic, intrusive, and metamorphic rocks (Fig. 2a) (Sgrosso, 1974). The clastic deposits are unconformably overlain by well-bedded lower Messinian calcarenites (Fig. 2a). Intercalated within the clastic deposits are hundreds of olistoliths, from a few dm^3 to several thousands of m^3 in volume. Olistoliths consist of Mesozoic-Cenozoic limestones and exotic rocks not exposed in the local sedimentary succession (hereafter named exotic olistoliths), such as marbles and recrystallized carbonates as well as volcanic, intrusive, and metamorphic rocks, and deep basinal Paleocene limestone blocks (Sgrosso, 1974; Di Girolamo et al., 2000; Vitale et al., 2018). The total thickness of the upper Tortonian-lower Messinian succession is ~800 m (Smeraglia et al., 2019).

2.3 The Mt. Massico mélange

The about ~150 m thick basal portion of the clastic deposits and the underlying hemipelagic marls are strongly deformed, showing a block-in-matrix fabric typical of tectonic mélanges (Fig. 2a,b; Vitale et al., 2018; Smeraglia et al., 2019). Based on new geological mapping (see also Vitale et al., 2018 for new stratigraphic constraints), structural analysis, U-Pb dating (syn-tectonic calcite ages of 10.5 ± 2.5 My, 7.0 ± 1.6 My, and 5.1 ± 3.7), and thermal modelling constrained by mixed layers illite-smectite, Smeraglia et al. 2019 proposed that the Mt. Massico tectonic mélange developed, since late Messinian times, by out-of sequence thrusting of multiple thrust sheets above the clastic deposits located in the backlimb of the Mt. Massico anticline (Fig. 9a-c) and by localization of deformation at the base of clastic deposits. In this context, the original stratigraphic boundary between the clastic deposits/hemipelagic marls deposits and the underlying limestones was sheared as a décollement horizon and an intra-wedge tectonic mélange developed due to the strong rheological contrast between the weak clastic deposits and the competent limestones. This mélange is characterized by a pervasive S-C and S-CC' fabrics showing a coherent transport direction towards ESE, accommodated by partitioned reverse and dextral transpressive tectonics (Fig. 2a; Smeraglia et al., 2019).

3. Methods

Aiming at characterize the structurally-controlled fluid circulation and the geochemical signature of the syn-tectonic fluids in the transition from the undeformed host rock to the tectonic mélange formation, we focused our structural and geochemical studies within the San Sebastiano and Mt. Cicoli areas (Fig. 2). In these areas, it is in fact possible to observe the progressive transition from poorly deformed clastic deposits to moderately and strongly deformed parts of the tectonic mélange along the boundary with the underlying bryozoan-rich limestones of the Cusano Fm. (Fig. 2a). To achieve this purpose we integrated: (1) geological field mapping at 1:10,000 scale, and available maps (Billi et al., 1997; Vitale et al., 2018; Smeraglia et al., 2019), to unravel the structural architecture and the deformation history of the intra-wedge tectonic mélange; (2) microstructural (optical microscope) analyses to unravel the deformation mechanisms acting during mélange generation; (3) Stable carbon and oxygen and carbonate clumped isotopes to reconstruct the origin and precipitation temperatures of the paleofluid circulating during mélange generation; (4) H_2O+CO_2, N_2, and minor gaseous species (He, Ne, and Ar concentrations and isotope ratios) in fluid inclusions on previously U-Pb dated syn-tectonic carbonate samples/veins (ages of 10.5 ± 2.5 My, 7.0 ± 1.6 My, and 5.1 ± 3.7; Smeraglia et al., 2019) . Sample preparation and analytical details are described in the Supplementary Material.

4. Results

4.1 Outcrop observations

A progressive transition in shear strain localization is observed when moving across strike along the studied area. Within the poorly deformed clastic deposits, bedding is still observable (Fig. 3a,b). The competent sandstones beds and the marly-shaly interbeds are gently folded and/or cut by low-displacement reverse faults displaying a ramp-and-flat geometry, with the flat segment located within marly and shaly interbeds (Fig. 3b). The marly and shaly interbeds are characterized by a weak and bedding-parallel scaly foliation (Fig. 3a,b); however, in places, an incipient S-C fabric characterized by bedding-parallel S planes and bedding-oblique C planes occurs dismembering the sandstone interbeds (Fig. 3a).

We recognized a up ~100 m-thick zone, referred as moderately deformed zone of the tectonic mélange, exposed within a diffuse boundary between the poorly deformed clastic deposits and the strongly deformed part of the tectonic mélange (Fig. 2). This zone is characterized by still detectable primary structures such as bedding, but competent strata (i.e. sandstones and calcarenites interbeds) show pinch-and-swell and boudin-like geometries. Pervasive and anastomosing bedding-parallel scaly foliation occurs within marly and shaly interbeds (Fig. 3c,d) and, in places, S-C fabrics can be observed (Fig. 3e). With increasing deformation, primary foliation is dismembered and relicts of bedding are scattered within the scaly foliation generating a block-in-matrix fabric (Fig. 3d-e). In particular, such relicts show bedding-perpendicular calcite veins (Fig. 3d,e).

The strongly deformed part of the tectonic mélange, up to ~50 m-thick, shows well-developed S-C and S-CC' tectonites and sedimentary structures are completely obliterated by tectonic fabric (Figs. 3f-h and 4a,b). In particular, the WNW- to WSW-dipping S- and C-surfaces show dip angles ranging ~60°-70° and ~10°-30°, respectively, with kinematic indicators showing mainly reverse dip-slip to right-lateral transpressional movements (Fig. 2a). Marls and shales are affected by S-C foliations and clasts of competent rocks (i.e. sandstones and calcarenites) are deformed in sigmoidal-lozenge-shaped structures consistent with the overall sense of shear (Figs. 3f-g and 4a-c). Stylolites and slickenfibers are aligned parallel respect to S and C planes, respectively, whereas sigmoidal clasts of competent rocks are permeated by calcite veins (Figs. 3g,h and 4d).

With increasing deformation, the sigmoidal relicts of sedimentary structures are progressively thinned and completely obliterated by S-C foliation so that it is difficult to distinguish them from the pervasive scaly foliation at the naked eye (Fig. 4c). In places, foliated marls and shales wrap olistoliths inherited from clastic deposits. The olistoliths preserve their original (from irregular to rounded) shapes, generating a block-in-matrix fabric (Fig. 4e-g). Convolute/contorted foliations also occur (Fig. 4h). Their origin is not clear and it cannot be excluded that they may be relicts of soft sediment (fluid escape) structures. When observable, the boundary between the tectonic mélange and the underlying bryozoan-rich limestones (not affected by deformation and with sedimentary structures and fossils still recognizable) is sharp.

4.2 Microstructural observations

We focused our microstructural observations on the strongly deformed parts of the tectonic mélange, with special focus on the sigmoidal-lozenge clasts of competent rocks (i.e. sandstones and calcarenites), since they are cohesive and can be easily cut for thin section preparation.

The sigmoidal-lozenge clasts are characterized by pervasive stylolites, parallel to S, C, and C' planes (Fig. 5a-c). Stylolites evolve from rough, teeth-shaped, and indented morphology (Figs. 5a-c and 6a-b) to smooth, continuous, and thick (up to 1 mm) dissolution seams (Figs. 5a-c and 6c) filled by insoluble material (i.e. clay minerals and oxides), small clasts of host rock limestones, and fragments of calcite veins (Fig. 6c). Stylolites and dissolution seams bound sigmoids defining a fabric sub-parallel to S, C, and C' planes (Figs. 5a-c and 6a,b). Sigmoids consist of host rock commonly with deformed microfossils, and/or reworked calcite veins (Fig. 6a,b).

We identify fibrous and blocky calcite veins. Fibrous veins are oriented perpendicular to stylolites ad are characterized by fibrous crystals perpendicular to vein margins (Fig. 6 d-f). Crystals are deformed by stylolites (Figs. 6d-f and 7a). The slickenfibers observed at the outcrop scale along S, C, and C' planes are characterized, at the microscale, by fibrous veins located along stylolite jogs, characterized by fibrous crystals parallel to stylolites (Fig. 6b,f). In places, fibrous veins occur within thick dissolution seams (Fig. 7a,b). In this case, vein margins and fibrous crystals are roughly parallel and perpendicular to dissolution seam margins, respectively (Fig. 7a,b). Blocky veins are filled by blocky to elongated-blocky calcite crystals and are oriented parallel, perpendicular, or oblique to stylolites (Fig. 7c,d).

Concerning the relative timing of structures, we observed mutual crosscutting relationships between veins and stylolites (Figs. 5c and 7f). In particular, blocky veins perpendicular to stylolites cut or are deformed by stylolites and/or by blocky/fibrous veins oriented oblique to stylolites (Figs. 5 and 7c-f). Fibrous veins parallel and/or perpendicular to stylolites are deformed by stylolites and/or by blocky veins oriented oblique to stylolites (Figs. 5, 7a,b, and 6d-f)

4.3 Stable and clumped isotopes

Results from stable and clumped isotopes analyses are shown in Fig. 8 and listed in Table S1 and S2. Results are reported in the conventional δ notation with respect to the Vienna Pee Dee Belemnite (VPDB) for $\delta^{13}C$ and Vienna Standard Mean Ocean Water (VSMOW) for $\delta^{18}O$. Clumped isotopes are reported in the Carbon Dioxide Equilibrium Scale (Dennis et al. 2011).

The host rock $\delta^{13}C$ and $\delta^{18}O$ values, measured on limestones interbeds within clastic deposits, range between -0.5‰ and +1.5‰, and between +26‰ and +29.5‰, respectively. Such values are typical of Miocene marine carbonates in the Apennines, Italy (e.g., Hilgen et al., 2005).

Blocky veins $\delta^{13}C$ and $\delta^{18}O$ values range between 0‰ and +0.8‰ and between +22.3‰ and +27‰, respectively, with one blocky vein showing $\delta^{13}C$ and $\delta^{18}O$ values overlapping those of the host rock. Fibrous veins $\delta^{13}C$ and $\delta^{18}O$ values range between -0.4‰ and +1.6‰ and between +22.4‰ and +27.8‰, respectively. Three fibrous veins show $\delta^{13}C$ and $\delta^{18}O$ values overlapping those of the host rock. Overall, both blocky and fibrous veins show $\delta^{13}C$ values overlapping with those of the host rock and an average $\delta^{18}O$ depletion of ~4‰ respect to the host rock.

Clumped-isotope data from blocky veins (four samples) and fibrous veins (five samples) yields $\Delta 47$ values between 0.424 and 0.482 (Table S2). These values correspond to temperatures between 108 ± 13 °C and 147 ± 20 °C (Fig. 8b and Table S1), using the equation of Bernasconi et al. (2018). The calculated $\delta^{18}O$ paleofluid compositions, using the O'Neil et al. (1969) equation developed for calcite precipitation temperature in the 0-500 °C range, range between 9.1‰ and 13.7‰ (Fig. 8b and Table S1).

4.4 Noble gas analysis

The concentrations of CO_2+H_2O, N_2, light noble gases (He, Ne, Ar), and $^{3}He/^{4}He$, $^{4}He/^{20}Ne$, $^{40}Ar/^{36}Ar$ isotopic ratios in fluid inclusions hosted in syntectonic calcite veins (samples 239, 257 and 260) are reported in Table S3.

CO_2+H_2O and N_2 show concentrations ranging between 1.1x10^{-6} and 8.3x10^{-6} mol/g and between 3.1x10^{-7} and 6.7x10^{-7} mol/g, respectively. The N_2/Ar ratios range between 3092 and 3633. These values are much more higher than the N_2/Ar ratio in the atmosphere (84.1) and the N_2/Ar ratio in air-saturated water at standard temperature and pressure (38). The $^{40}Ar/^{36}Ar$ ratios vary from 367.3 to 389.9, slightly higher than the $^{40}Ar/^{36}Ar$ ratio in atmosphere (298.6).

He/Ar and He/N_2 ratios range between 0.06-0.14 and 2.1-3.8x10^{-5}, respectively, and are 1-2 orders of magnitude higher than the theoretical values in the atmosphere and in the air-saturated water. The $^{4}He/^{20}Ne$ ratios range between 51.7 and 96.5 and are more than two orders of magnitude higher than the typical $^{4}He/^{20}Ne$ ratio in air saturated water (0.268), consistently with fluids trapped at great depth. All these ratios testify an excess of He and N_2 respect to the typical concentrations in atmosphere-derived fluids. The $^{3}He/^{4}He$ ratios, corrected for the air contamination (R/Ra ratio) range between 0.05 and 0.09, consistently with those of crustal fluids, thus excluding a contribution of He derived from atmospheric air and ^{3}He from the mantle (Fig. 8d).

The $^{3}He/^{4}He$ and $^{40}Ar/^{36}Ar$ ratios are useful tracers to ascertain the origin of the fluids producing the mineralization. However, one condition is that these materials must contain volatiles trapped during precipitation processes and that their isotopic compositions have not been modified over time. Significant post precipitation processes that may affect the noble gases content in the fluid inclusions regard the addition of (1) ^{4}He, ^{40}Ar produced from the radiogenic decay of U, Th and K, and (2) cosmogenic ^{3}He derived from the exposure to cosmic ray.

In order to estimate the contribution of radiogenic ^{40}Ar into the fluid inclusions, we computed the $^{40}Ar^*$, which is the amount of ^{40}Ar corrected for the atmospheric contributions ($^{40}Ar^* = {}^{40}Ar/^{36}Ar_{Measured} - {}^{40}Ar/^{36}Ar_{Atmosphere} \times {}^{36}Ar_{Measured}$). The amounts of $^{40}Ar^*$ range between 8.99 x 10^{-11} to 1.38 x 10^{-10} mol/g (Table S3). The amounts of the measured ^{4}He and measured $^{40}Ar^*$ do not show any correlations with the ages of the veins (Fig. S1a,b), thus excluding the accumulation of radiogenic He and Ar produced in the veins by the U, Th and K decay during time.

All calcite veins have been collected in outcrops whose time of exposure to the cosmic ray at the surface is not evaluable; hence, the potential contribution of cosmogenic ^{3}He trapped in the fluid inclusions is difficult to be assessed. However, there is no correlation between the amount of ^{3}He and the ages of calcite veins (Fig. S1c), which can supports a progressive accumulation over time of cosmogenic ^{3}He and subsequent migration into the fluid inclusions.

On the basis of the average U and Th amounts in the veins of calcite (1.58 and 2.28 ppm for sample 257; 0.35 and 0.01 ppm for sample 239; 0.17 and 0.02 ppm for sample 260; Table S4) is possible to compute the potential $^{4}He/^{40}Ar^*$ ratio produced by the decay of U and Th. The computed $^{4}He/^{40}Ar^*$ ratios range between 10 and 100. These values are much higher than the same ratios in the fluid inclusions (0.61, 0.35, and 0.40 for samples 257, 239, and 260, respectively, Table S3). This suggests that the fluid inclusions are not modified by the contributions of both of radiogenic ^{4}He and ^{40}Ar produced within the rocks. We conclude that the isotopic ratios of He and Ar in the fluid inclusions are representative of the pristine isotopic signatures of the trapped fluids.

5. Discussion

5.1 Mélange evolution and deformation mechanisms

Since late Messinian times, the Mt. Massico tectonic mélange developed by out-of sequence thrusting of multiple thrust sheets above the clastic deposits and by localization of deformation at the base of clastic deposits (Fig. 9a-c; Smeraglia et al., 2019). Therefore, when out-of sequence deformation initiated, WSW-ENE shortening affected W-SW-dipping (30°-55°) Meso-Cenozoic carbonates and middle-upper Miocene clastic deposits, tilted by previous thrust-related folding (Fig. 2a,b and 9b; Smeraglia et al., 2019). In this context, both layer-perpendicular/oblique shortening and layer-parallel extension occurred in the early phases of deformation (Fig. 10a,b). Layer-perpendicular/oblique shortening was driven by sub-horizontal tectonic compression and produced bedding-parallel foliation by pressure-solution and stylolites generation in the marly and shaly interbeds (Figs. 3a,b). Layer-parallel extension produced dismembering, boudinage, and fracturing of competent bedding (i.e. sandstones and calcarenites interbeds; Fig. 3c).

With increasing deformation, the hemipelagic marls between the clastic deposits and bryozoan-rich limestones were scraped off and mixed within the base of clastic deposits, the competent beds were almost completely dismembered, although some relicts of bedding were scattered within the shaly/marly matrix (Figs. 3d, 4e-g, and 10c,d). In this framework, S-C tectonites and block-in-matrix fabric developed within the strongly deformed parts of the tectonic mélange by brittle-ductile processes such as pressure-solution, fracturing/veining, and frictional sliding, with absence of evident cataclasis of the host rock (Fig. 10c,d). The absence of cataclasis is related to the occurrence of widespread pressure solution processes, triggered and enhanced by clay-rich host rocks (marls and shales; Renard et al., 1997), which promoted the dissipation of tectonic stress through host rock dissolution, at slow strain rates rather, than frictional processes (i.e. fracturing, grain rotation, abrasion) commonly occurring during cataclasis in competent rocks, such as pure carbonates (e.g. Billi, 2010). In particular, pressure-solution was more pervasive in weak marly and shaly interbeds than in calcarenite interbeds, producing a network of stylolites aligned along S, C, and C' planes. Stylolites developed through host rock dissolution and insoluble materials (i.e. mainly phyllosilicates) concentrated within dissolution seams (Figs. 3f-h and 4a-c) (e.g. Tesei et al., 2013). Fracturing/veining processes, coupled with pressure-solution, affected the relicts of competent rocks (Figs. 3f-h, 4a-d, and 10c,d). These types of deformation mechanisms commonly occur during tectonic mélange generation (e.g., Festa et al., 2012 for review).

5.2 Vein development within the mélange

The occurrence of veins perpendicular to stylolites suggests that both structures formed under the same stress regime, characterized by compression sub-perpendicular to the stylolites, thus generating mode I vein opening perpendicular to stylolites to regulate their evolution through time (Figs. 5a-c, 6d, 7c-f, and 11; e.g., Gratier et al., 2013). Veins parallel to stylolites (Figs. 6f and 7a,b) indicate opening direction parallel to the maximum compression direction and suggests vein opening under an unfavorable stress regime (i.e. opening direction should be perpendicular with respect to the maximum principal stress). In particular, development of fibrous veins (shear veins/slickenfibers) characterized by fibrous crystals perpendicular to the maximum principal stress have been observed in tectonic mélange and have been related to shear along pre-existing weak planes such as clay-rich stylolites, assisted by fluid overpressure (Fagereng et al., 2010). Alternatively, the unfavorable orientations between veins and tectonic stresses can be explained by episodic stress rotation within the mélange, vein reworking/rotation during deformation, and/or overpressured fluids that may have opened pre-existing discontinuities, such as stylolites. Although stylolites are commonly considered efficient barriers to fluid flow (Toussaint et al., 2018 for review), veins developed along stylolites (Fig. 7a,b) suggest that they can be preferential pathways for fluid redistribution, consistently with recent experimental and field evidence (e.g., Heap et al., 2014; Bruna et al., 2019). In particular, the low-permeability network generated by stylolites can favor fluid overpressure rise.

Stylolite steps filled by calcite crystals (Fig. 6f) suggest opening of voids (i.e. extensional pull-apart) due to slip along undulated stylolites, which promoted calcite precipitation into newly created space, a mechanism commonly occurring during slickenfiber generation (e.g. Fagereng and Byrnes, 2015). This mechanism indicates that frictional sliding occurred along S-, C-, and C'-planes by smoothing the tooth-shaped margins of stylolites and slip along thick clay-rich dissolution seams (Fig. 10d; Tesei et al., 2013).

Fibrous crystals (Figs. 6d-f and 7a,b) generated through multiple and micrometer-thick opening increments (e.g., Bons et al., 2012), is incompatible with coeval growth of blocky and/or elongated-blocky crystals that typically develop in fluid-filled spaces generated by a single opening increment larger than that of fibrous veins (e.g. Bons et al., 2012). These different deformation mechanisms suggest various slip rates and deformation behaviors within the mélange. Continuous deformation may have occurred within the ductile clay-rich matrix, while discontinuous slip may have occurred during fibrous and blocky vein generation in more competent carbonate-rich blocks (e.g. Fagereng, 2011). In particular, fibrous veins suggest discontinuous creep at very slow slip rates. On the contrary, impulsive deformation at high and fast slip rates may have occurred during blocky vein generation generated by impulsive crackle-like brecciation (e.g. Woodcock et al., 2014; Fagereng and Byrnes, 2015). In both cases, fracturing/veining were probably assisted by fluid overpressure, consistently with crackle-like brecciation (Fig. 5) and the dense network of clay-rich stylolites, which may have created impermeable barriers and fluid pressure rises over time (Moore and Vrolijk, 1992).

Crosscutting relationships between structures show recurrent cycles of mutually overprinting brittle (fracturing/veining and frictional sliding) and ductile (pressure-solution) processes indicate a multiphase deformation history (Figs. 5, 6, 7, and 11). Stylolite formation through fibrous veins (Fig. 6d,e) indicate the interruption of the fracturing event and the onset of a new pressure-solution phase, indicating alternating phases of frictional sliding and dissolution processes (Fig. 11; e.g., Tesei et al., 2013; Giorgetti et al., 2016). Reworking of inherited veins also occurred (Figs. 10b and 11). This inference is consistent with previous U/Pb dating on three calcite-filled veins within the tectonic mélange showing ages of 10.5 ± 2.5 My, 7.0 ± 1.6 My, and 5.1 ± 3.7 My, respectively indicating multiple events of calcite precipitation during deformation (Smeraglia et al., 2019).

5.3 Fluid source and syn-tectonic fluid circulation

Geochemical data indicate calcite precipitation at temperatures between ~100 and ~150 °C from retained pore water, such as marine water retained in the clastic sediments during diagenesis, modified or completely buffered by isotope exchange with the host rock. We base this interpretation on the following evidence:

(1) The calculated δ^{18}O paleofluid composition, which was in equilibrium with the calcite at the time of mineral growth, ranges between +9.1‰ and +13.7‰ (Fig. 8b). These values indicate ^{18}O enrichment suggesting extensive oxygen exchange between the fluids and the limestone interbeds of clastic deposits. In particular, most of the calculated δ^{18}O paleofluid compositions ranging between +9‰ and +11‰ (Fig. 8b), indicate high water/rock ratios and paleofluids with nearly constant δ^{18}O composition, which were responsible for calcite precipitation at progressive increasing temperatures from 108 to 146 °C (Fig. 8b).

(2) Data from fluid inclusions in veins suggest an excess of radiogenic He and Ar in fluids circulating during the precipitation of calcite, indicating a source of both He and Ar other than the atmosphere and the mantle. In particular, the ^{3}He/^{4}He ratios are lower than 0.1 R/Ra (Fig. 8d and Table S3) indicating a crustal fluid. In addition, these values are similar to those of crustal-derived fluids (with limited or negligible mantle contribution) enriched in ^{4}He recorded in natural gaseous emissions of the central-northern Apennines (e.g., Buttitta et al., 2020).

(3) The R/Ra ratios of calcite veins are lower than those calculated from actual springs along the Mt. Massico ridge and related to the Roccamonfina volcano (0.39 Ra to 1.99 Ra, typical of mantle-derived fluids; Cuoco et al., 2017), located ~20 towards the NE respect to the study area (Fig. 1), thus excluding the contribution of mantle-derived fluids circulating within the tectonic mélange. In addition, the volcanic activity at Roccamonfina occurred between ~0.6 and ~0.1 My, ~5 My after the latest tectonic activity documented at Mt. Massico (U-Pb vein dated at 5.1 ± 3.7 My, Smeraglia et al., 2019), further excluding the mixing of mantle-derived fluids from Roccamonfina with crustal fluids circulated within the tectonic mélange.

However, we cannot completely exclude that also meteoric water partly infiltrated within the tectonic mélange during deformation and/or exhumation, and was modified by ^{18}O isotope exchange with the host rock, acquiring the calculated $\delta^{18}O$ paleofluid composition.

Based on geochemical and geological data, we suggest that syn-tectonic fluid circulation within the Mt. Massico mélange occurred in a closed system, without a strong connection with external reservoirs (i.e. meteoric or mantle-derived fluids). We therefore propose that during sedimentary and tectonic burial, marine-derived fluids trapped within sandstones and shale interlayers were progressively heated up to 147 °C. During deformation, regional tectonic shortening caused sandstones and shale compaction, porosity reduction, and, eventually, expulsion of previously stored fluids and calcite precipitation into newly-created fractures. In addition, the progressive smectite to illite conversion through mixed layers illite-smectite occurring from temperatures of 60-70 °C to 210 °C (Aldega et al., 2017), may have triggered additional source for local fluids due to water expulsion during clay dehydration (e.g. Moore and Vrolijk, 1992).

Syn-tectonic fluid circulation in closed systems has been already observed in tectonic mélange exposed in various fold-and-thrust belts (i.e. Apennines, Pyrenees) developed within sedimentary succession with alternating of sandstones, marls, and shale (e.g., Vannucchi et al, 2010; Gabellone et al., 2013; Lacroix et al., 2014). The Mt. Massico mélange did not acted as a conduit for external fluids as observed within intra-wedge tectonic mélange in the Apennines (Meneghini et al., 2012), Sicilian (Dewever et al., 2013), Thailand (Hansberry et al., 2015), and Japan (Raimbourg et al., 2015) fold-and-thrust belts. We explain this difference suggesting that meso- and microstructures of the Mt. Massico mélange, such as clay-rich stylolites and marls-shale interlayers (Figs. 3, 4, 6, and 7), created efficient low-permeability barriers, which prevented the ingress of fluids from external reservoirs. Otherwise, the occurrence of regional thrusts, both below and above the Mt. Massico tectonic mélange, may have acted as regional conduits for the drainage of external fluids within the accretionary wedge and away from the tectonic mélange.

We observe an inverse correlation between fluid temperature and ages of calcite veins, showing an increase of calcite precipitation temperature with decreasing ages (Fig. 8c; U-Pb data from Smeraglia et al., 2019). The vein formed at 10.5 ± 2.5 My at temperature of 108 °C suggests an early phase of deformation during wedge accretion (e.g. Tavani et al., 2015). This is not consistent with the burial history proposed by Smeraglia et al. (2019), which shows much lower temperature for the base of the clastic deposits than that recorded by clumped isotopes before the onset of thrusting at 10.5 ± 2.5 My (i.e. Tortonian time; see Fig. 13a in Smeraglia et al., 2019). This can be explained by the lateral and upward migration of deep-seated warm fluids, previously stored in areas already affected by tectonic burial (e.g., Minshull et al., 1989), which circulated within the clastic deposits at shallow depths during the Tortonian. The occurrence pre-Tortonian tectonic burial is highlighted by the borehole stratigraphy of Mara 01 well, located towards the SW respect the Mt. Massico, showing the thrusting of Triassic deposits above Paleocene-Eocene deposits (See Fig. 2 in Smeraglia et al., 2019)

Veins formed at 7.0 ± 1.6 My and 5.1 ± 3.7 My at temperatures of 121 and 147 °C, respectively, are consistent with the progressive burial due to thrust sheet emplacement above the mélange (Smeraglia et al., 2019). However, we point out that most of precipitation temperatures are fully consistent with the maximum burial temperature of 140 °C at depths of ~4 km experienced by the mélange, calculated by 1D thermal modelling constrained by mixed layers illite-smectite (Smeraglia et al., 2019). This indicates that fluid expulsion occurred under maximum burial condition, suggesting that tectonic overburden promoted and/or triggered fluid overpressure and hydrofracturing.

Conclusions

Structural and microstructural observations combined with geochemical data (stable and clumped isotopes and isotope composition of noble gases in fluid inclusions of calcite veins) along the carbonate/shale-bearing tectonic mélange within the central Apennines accretionary wedge (Mt. Massico mélange) show that:

(1) Intra-wedge tectonic mélange generates along pre-existent intra- and interformational rheological contrast occurring along carbonate/shale sedimentary successions. In particular, deformation is localized at the boundary between weak (Tortonian clastic deposits and hemipelagic marls) and competent (Meso-Cenozoic limestones) rocks. The development of tectonic mélange occurred by disruption of the primary bedding, mixing, and deformation of relicts of competent blocks (i.e., olistoliths and relicts of competent strata) within a weak matrix (i.e., deformed shaly and marly interbeds), through recurrent cycles of mutually overprinting brittle (fracturing/veining and frictional sliding) and ductile (pressure-solution) processes, indicating a polyphase deformation history characterized by fast to slow strain rates.

(2) The geochemical signatures of syn-tectonic calcite veins indicate calcite precipitation from warm (108-147 °C) and modified pore fluids, by isotope exchange with the local host rock. Fluid circulation occurred mostly in a closed system dominated by the expulsion and redistribution of pore fluids trapped during sedimentation/diagenesis and/or derived by clay dehydration processes (at T > 120 °C), without the interaction of externally derived fluids (i.e. meteoric and/or mantle-derived fluids). A minor contribution from lateral-upward migration of deep-seated warm fluids, previously stored in areas affected by tectonic burial located towards the SW from the Mt. Massico, is inferred in the early phase of the deformation of tectonic mélange. Low-permeability barriers, generated by clay-rich stylolites, promoted the generation of fluid overpressure, which were mostly expelled at maximum burial conditions (T 140 °C and depth of ~4 km) in the final stage of mélange deformation. Therefore, clay-rich intra-wedge tectonic mélanges, along décollement zones, may generate efficient barriers within accretionary wedges for vertical and lateral redistribution of fluids from reservoirs outside the mélange.

We highlight that the integration of geochemical (stable and clumped isotopes, analysis of gaseous species in fluid inclusions) and geochronological (U-Pb dating) methods can be a powerful approach to better constrain the burial-thermal evolution and the fluid storage capacity of fold and thrust belts and sedimentary basins, including the associated fault network.

Acknowledgements

This work has been funded by: Progetti di Ateneo Sapienza 2017 to E. Carminati, Progetti di Ateneo Sapienza 2016 to L. Aldega, and Progetto di Avvio alla Ricerca 2016 Sapienza to L. Smeraglia. We thank D. Mannetta and TSLab & Geoservices for thin sections, A. Conti, F. Di Fiore, and S. Fabbi constructive discussions and help during fieldwork and sampling and M. Jaggi for the isotope analyses. We are grateful to M. Tantillo for analyzing the chemistry of CO_2+H_2O, N_2, and the isotope composition of light noble gases.

References

Aldega L., Carminati E., Scharf A., Mattern F. & Al-Wardi M. (2017). Estimating original thickness and extent of the Semail Ophiolite in the eastern Oman Mountains by paleothermal indicators. *Marine and Petroleum Geology, 84*, 18-33.

Bernasconi, S. M., Müller, I. A., Bergmann, K. D., Breitenbach, S. F., Fernandez, A., et al. (2018). Reducing uncertainties in carbonate clumped isotope analysis through consistent carbonate-based standardization. *Geochemistry, Geophysics, Geosystems*, *19*(9), 2895-2914.

Billi, A. (2010). Microtectonics of low-P low-T carbonate fault rocks. *Journal of Structural Geology*, *32*(9), 1392-1402.

Billi, A., Bosi, V., & De Meo, A. (1997). Caratterizzazione strutturale del rilievo del M. Massico nell'ambito dell'evoluzione quaternaria delle depressioni costiere dei fiumi Garigliano e Volturno (Campania settentrionale). Il Quaternario, 10(1), 15–26.

Bons, P. D., Elburg, M. A., & Gomez-Rivas, E. (2012). A review of the formation of tectonic veins and their microstructures. *Journal of Structural Geology*, *43*, 33-62.

Bruna, P. O., Lavenu, A. P., Matonti, C., & Bertotti, G. (2019). Are stylolites fluid-flow efficient features?. *Journal of Structural Geology*, *125*, 270-277.

Buttitta, D., Caracausi, A., Chiaraluce, L., Favara, R., Morticelli, M. G., & Sulli, A. (2020). Continental degassing of helium in an active tectonic setting (northern Italy): the role of seismicity. *Scientific Reports*, *10*(1), 1-13.

Carminati, E., Lustrino, M., & Doglioni, C. (2012). Geodynamic evolution of the central and western Mediterranean: Tectonics vs. igneous petrology constraints. Tectonophysics, 579, 173–192. https://doi.org/10.1016/j.tecto.2012.01.026

Codegone, G., Festa, A., & Dilek, Y. (2012). Formation of Taconic mélanges and broken formations in the Hamburg Klippe, central Appalachian orogenic belt, eastern Pennsylvania. *Tectonophysics*, *568*, 215-229.

Cuoco, E., Minissale, A., Tamburrino, S., Iorio, M., & Tedesco, D. (2017). Fluid geochemistry of the Mondragone hydrothermal systems (southern Italy): water and gas compositions vs. geostructural setting. *International Journal of Earth Sciences*, *106*(7), 2429-2444.

Dennis, K. J., Affek, H. P., Passey, B. H., Schrag, D. P., & Eiler, J. M. (2011). Defining an absolute reference frame for 'clumped'isotope studies of CO2. *Geochimica et Cosmochimica Acta*, *75*(22), 7117-7131.

Dewever, B., Swennen, R., & Breesch, L. (2013). Fluid flow compartmentalization in the Sicilian fold and thrust belt: Implications for the regional aqueous fluid flow and oil migration history. *Tectonophysics*, *591*, 194-209.

Di Girolamo, P., Sgrosso, I., De Gennaro, R., & Giurazzi, S. (2000). Metamorphic rocks in Campania (southern Italy); The "Mondragone marbles". Bollettino della Societa Geologica Italiana, 119(3), 761–766.

Fagereng, Å. (2011). Fractal vein distributions within a fault-fracture mesh in an exhumed accretionary mélange, Chrystalls Beach Complex, New Zealand. *Journal of Structural Geology*, *33*(5), 918-927.

Fagereng, Å., & Byrnes, G. (2015). A range of fault slip styles on progressively misoriented planes during flexural-slip folding, Cape Fold Belt, South Africa. *Journal of Structural Geology*, *70*, 156-169.

Fagereng, Å., & Cooper, A. F. (2010). The metamorphic history of rocks buried, accreted and exhumed in an accretionary prism: An example from the Otago Schist, New Zealand. Journal of Metamorphic Geology, 28(9), 935–954. https://doi.org/10.1111/j.1525-1314.2010.00900.x

Fagereng, Å., Remitti, F., & Sibson, R. H. (2010). Shear veins observed within anisotropic fabric at high angles to the maximum compressive stress. *Nature Geoscience*, *3*(7), 482.

Festa, A., Dilek, Y., Pini, G. A., Codegone, G., & Ogata, K. (2012). Mechanisms and processes of stratal disruption and mixing in the development of mélanges and broken formations: Redefining and classifying mélanges. *Tectonophysics*, *568*, 7-24.

Gabellone, T., Gasparrini, M., Iannace, A., Invernizzi, C., Mazzoli, S., & D'antonio, M. (2013). Fluid channeling along thrust zones: the Lagonegro case history, southern Apennines, Italy. *Geofluids*, *13*(2), 140-158.

Giorgetti, C., Collettini, C., Scuderi, M. M., Barchi, M. R., & Tesei, T. (2016). Fault geometry and mechanics of marly carbonate multilayers: An integrated field and laboratory study from the Northern Apennines, Italy. *Journal of Structural Geology*, *93*, 1-16.

Gratier, J. P., Thouvenot, F., Jenatton, L., Tourette, A., Doan, M. L., & Renard, F. (2013). Geological control of the partitioning between seismic and aseismic sliding behaviours in active faults: Evidence from the Western Alps, France. *Tectonophysics*, *600*, 226-242.

Hansberry, R. L., Collins, A. S., King, R. C., Morley, C. K., Giże, A. P., Warren, J., ... & Hall, P. A. (2015). Syn-deformation temperature and fossil fluid pathways along an exhumed detachment zone, khao khwang fold-thrust belt, Thailand. *Tectonophysics*, *655*, 73-87.

Heap, M. J., Baud, P., Reuschlé, T., & Meredith, P. G. (2014). Stylolites in limestones: Barriers to fluid flow?. *Geology*, *42*(1), 51-54.

Hilgen, F., Aziz, H. A., Bice, D., Iaccarino, S., Krijgsman, W., Kuiper, K., ... & Zachariasse, W. J. (2005). The global boundary stratotype section and point (GSSP) of the Tortonian stage (Upper Miocene) at Monte Dei Corvi. *Episodes-Newsmagazine of the International Union of Geological Sciences*, *28*(1), 6-17.

Lacroix, B., Travé, A., Buatier, M., Labaume, P., Vennemann, T., & Dubois, M. (2014). Syntectonic fluid-flow along thrust faults: Example of the South-Pyrenean fold-and-thrust belt. *Marine and Petroleum Geology*, *49*, 84-98.

Luiso, P., Paoletti, V., Nappi, R., La Manna, M., Cella, F., Gaudiosi, G., & Iorio, M. F. M. (2018). A multidisciplinary approach to characterize the geometry of active faults: The example of Mt. Massico, Southern Italy. Geophysical Journal International, 213(3), 1673–1681. https://doi.org/10.1093/gji/ggy080

Malinverno, A., & Ryan, W. B. (1986). Extension in the Tyrrhenian Sea and shortening in the Apennines as result of arc migration driven by sinking of the lithosphere. Tectonics, 5(2), 227–245. https://doi.org/10.1029/TC005i002p00227

Meneghini, F., Marroni, M., Moore, J. C., Pandolfi, L., & Rowe, C. D. (2009). The processes of underthrusting and underplating in the geologic record: Structural diversity between the Franciscan Complex (California), the Kodiak Complex (Alaska) and the Internal Ligurian Units (Italy). Geological Journal, 44(2), 126–152. https://doi.org/10.1002/gj.1144

Meneghini, F., Botti, F., Aldega, L., Boschi, C., Corrado, S., Marroni, M., & Pandolfi, L. (2012). Hot fluid pumping along shallow-level collisional thrusts: the Monte Rentella Shear Zone, Umbria Apennine, Italy. *Journal of Structural Geology*, *37*, 36-52.

Minshull, T., & White, R. (1989). Sediment compaction and fluid migration in the Makran accretionary prism. *Journal of Geophysical Research: Solid Earth*, *94*(B6), 7387-7402.

Moore, J. C., & Vrolijk, P. (1992). Fluids in accretionary prisms. *Reviews of Geophysics*, *30*(2), 113-135.

Morley, C. K., von Hagke, C., Hansberry, R. L., Collins, A. S., Kanitpanyacharoen, W., & King, R. (2017). Review of major shale-dominated detachment and thrust characteristics in the diagenetic zone: Part I, meso-and macro-scopic scale. Earth-Science Reviews, 173, 168–228. https://doi.org/10.1016/j.earscirev.2017.07.019

Mostardini, F., & Merlini, S. (1986). Appennino centroemeridionale. Sezioni geologiche e proposta di modello strutturale. Memorie della Societa Geologica Italiana, 35, 177–202.

O'Neil, J. R., Clayton, R. N., & Mayeda, T. K. (1969). Oxygen isotope fractionation in divalent metal carbonates. *The Journal of Chemical Physics*, *51*(12), 5547-5558.

Ogata, K., Pini, G. A., Carè, D., Zélic, M., & Dellisanti, F. (2012). Progressive development of block-in-matrix fabric in a shale-dominated shear zone: Insights from the Bobbio Tectonic Window (Northern Apennines, Italy). Tectonics, 31, TC1003. https:// doi.org/10.1029/ 2011TC002924

Raimbourg, H., Augier, R., Famin, V., Gadenne, L., Palazzin, G., Yamaguchi, A., & Kimura, G. (2014). Long-term evolution of an accretionary prism: The case study of the Shimanto Belt, Kyushu, Japan. *Tectonics*, *33*(6), 936-959.

Renard, F., Ortoleva, P., & Gratier, J. P. (1997). Pressure solution in sandstones: influence of clays and dependence on temperature and stress. *Tectonophysics*, *280*(3-4), 257-266.

Sgrosso, I. (1974). I rapporti tra la piattaforma carbonatica Campano-Lucana e la piattaforma Abruzzese-Campana al Monte Massico (Caserta). Bollettino della Societa Geologica Italiana, 93(4), 1197–1209.

Smeraglia, L., Aldega, L., Billi, A., Carminati, E., Di Fiore, F., Gerdes, A., ... & Vignaroli, G. (2019). Development of an Intrawedge Tectonic Mélange by Out-of-Sequence Thrusting, Buttressing, and Intraformational Rheological Contrast, Mt. Massico Ridge, Apennines, Italy. *Tectonics*, *38*(4), 1223-1249.

Tavani, S., Storti, F., Lacombe, O., Corradetti, A., Muñoz, J. A., & Mazzoli, S. (2015). A review of deformation pattern templates in foreland basin systems and fold-and-thrust belts: Implications for the state of stress in the frontal regions of thrust wedges. *Earth-Science Reviews*, *141*, 82-104.

Tesei, T., Collettini, C., Viti, C., & Barchi, M. R. (2013). Fault architecture and deformation mechanisms in exhumed analogues of seismogenic carbonate-bearing thrusts. *Journal of Structural Geology*, *55*, 167-181.

Toussaint, R., Aharonov, E., Koehn, D., Gratier, J. P., Ebner, M., et al. (2018). Stylolites: A review. *Journal of Structural Geology 114*, 163-195.

Vannucchi, P., & Bettelli, G. (2002). Mechanism of subduction accretion as implied from the broken formations in the Apennines, Italy. Geology, 30(9), 835–838. https://doi.org/10.1130/0091-7613(2002)030<0835:MOSAAI>2.0.CO;2

Vannucchi, P., Remitti, F., & Bettelli, G. (2008). Geological record of fluid flow and seismogenesis along an erosive subducting plate boundary. Nature, 451(7179), 699–703. https://doi.org/10.1038/nature06486

Vannucchi, P., Remitti, F., Bettelli, G., Boschi, C., & Dallai, L. (2010). Fluid history related to the early Eocene-middle Miocene convergent system of the Northern Apennines (Italy): Constraints from structural and isotopic studies. Journal of Geophysical Research, 115, B05405. https://doi.org/10.1029/2009JB006590

Vezzani, L., Festa, A., & Ghisetti, F. C. (2010). Geology and tectonic evolution of the Central-Southern Apennines, Italy, Special Paper (Vol. 469, pp. 1–58). America: Geological Society. https://doi.org/10.1130/2010.2469

Vitale, S., & Ciarcia, S. (2018). Tectono-stratigraphic setting of the Campania region (southern Italy). Journal of Maps, 14(2), 9–21. https:// doi.org/10.1080/17445647.2018.1424655

Vitale, S., Prinzi, E. D., Ciarcia, S., Sabbatino, M., Tramparulo, F. D. A., & Verrazzo, G. (2018). Polyphase out-of-sequence thrusting and occurrence of marble detritus within the wedge-top basin deposits in the Mt. Massico (southern Apennines): Insights into the late Miocene tectonic evolution of the central Mediterranean. International Journal of Earth Sciences. https://doi.org/10.1007/s00531-018-1664-0

Vrolijk, P., Myers, G., & Moore, J. C. (1988). Warm fluid migration along tectonic melanges in the Kodiak accretionary complex, Alaska. *Journal of Geophysical Research: Solid Earth*, *93*(B9), 10313-10324.

Woodcock, N. H., Miller, A. V. M., & Woodhouse, C. D. (2014). Chaotic breccia zones on the Pembroke Peninsula, south Wales: Evidence for collapse into voids along dilational faults. *Journal of Structural Geology*, *69*, 91-107.

Figure Captions

Figure 1. (a) Simplified geological map of the central-southern Apennines (Italy) showing main thrusts and location of the study area. **(b)** Schematic geological cross-section through the central-southern Apennines (modified after Mostardini and Merlini, 1986). (c) Geological cross-section through the Mt. Massico ridge (i.e., the study area).

Figure 2. (a) Detailed geological map of the southwestern part of the Mt. Massico ridge with location of key outcrops where the tectonic mélange is exposed. Schmidt nets (lower hemisphere) showing the attitude of S-C planes with related slip vectors within the tectonic mélange. Modified after Smeraglia et al. (2019) **(b)** Geological cross-sections across the Mt. Massico ridge.

Figure 3. Outcrop-scale structural features of the Mt. Massico tectonic mélange. **(a,b)** The poorly deformed clastic deposits showing bedding and incipient foliation. Note folded strata and low-displacement faults showing ramp and flat geometry. **(c)** The moderately deformed zone showing competent strata (i.e. sandstones and calcarenites interbeds) characterized by pinch-

and-swell and boudine-like geometries. **(d)** Relict of competent strata. **(d)** Detail of competent strata (Fig. 3c) showing veins perpendicular to bedding and S-C foliation. **(f,g)** The strongly deformed part of the tectonic mélange showing S-C foliation within marls and shale and relict of competent strata (limestones and sandstones) showing sigmoidal shapes. **(h)** Relict of competent limestones showing stylolites along S- and C-planes. Inset shows the Schmidt nets (lower hemisphere) showing the attitude of S-C planes with related slip vectors.

Figure 4. Outcrop-scale structural features of the Mt. Massico tectonic mélange. **(a-c)** The strongly deformed part of the tectonic mélange characterized by S-C and S-CC' tectonites within marls and shale and relict of competent strata (limestones and sandstones) showing sigmoidal shapes. **(d)** Relict of competent limestones showing a pervasive network of calcite veins. **(e-h)** Inherited competent (limestones) olistoliths scattered within the weak (marls and shale) scaly foliation, generating the block-in-matrix fabric typical of tectonic mélange. **(h)** Contorted and convoluted foliation within the S-C tectonite.

Figure 5. High-resolution hand sample scan of relicts of competent limestones showing sigmoidal shapes. Stylolites are aligned along S-, C- and C'-planes. Calcite veins are oriented parallel, perpendicular, and/or oblique with respect to stylolites. No stylolites affecting calcite veins and calcite veins cutting through stylolites occur.

Figure 6. Microstructures from the tectonic mélange. **(a-c)** Stylolites affecting host rock relicts and calcite veins. Note the insoluble materials (clays and oxides) filling up to 1-mm thick dissolution seams. **(d,e)** Fibrous veins characterized by fibrous calcite crystals with long axis oriented roughly parallel to stylolites. Note stylolites affecting fibrous veins. **(f)** Fibrous crystals developed along stylolites jogs along C-plane. Fibrous crystals with long axis oriented roughly parallel to stylolites.

Figure 7. Microstructures from the tectonic mélange. **(a,b)** Fibrous veins characterized by fibrous calcite crystals with long axis oriented perpendicular to stylolites. Note that this type of fibrous veins develop within stylolites. **(c,d,e,f)** Blocky veins characterized by blocky calcite crystals. Blocky veins are oriented parallel, perpendicular, and/or oblique respect to stylolites. Note stylolites affecting blocky veins and mutual crosscutting relationships between blocky veins.

Figure 8. (a) $\delta^{13}C$ (‰ V-PDB) versus $\delta^{18}O$ (‰ V-SMOW) diagram from blocky and fibrous veins and host rocks in the Mt. Massico tectonic mélange. Notice the average $\delta^{18}O$ depletion of ~4‰ between mélange-related mineralizations and host rock. **(b)** Oxygen isotope fractionation during equilibrium precipitation: $\delta^{18}O$ of fault-related mineralizations and paleofluid compositions (curves) as a function of temperature. The $\delta^{18}O$ calculated paleofluid compositions (between 9‰ and 14‰) indicate strong ^{18}O exchange with the local limestone host rock. Notice that warmer fluids have similar $\delta^{18}O$ paleofluid composition suggesting that the same paleofluid was the source for calcite precipitation at increasing temperatures and depths. **(c)** Temperature (°C, clumped isotopes) versus age (My, U-Pb dating, data from Smeraglia et al., 2019) diagram for three dated veins. Notice the increase in paleofluid temperature with decreasing ages, which indicates progressive tectonic burial during discontinuous thrust sheet emplacement through time. **(d)** $^{4}He/^{20}Ne$ ratio versus $^{3}He/^{4}He$ (R/Ra) ratio diagram. Note that the calcite veins are in the range of R/Ra values typical of crustal fluids of the central Apennines.

Figure 9. (a) Large-scale tectonic setting of the Apennine subduction (modified after Scrocca et al., 2005) and location of the Mt. Massico structure within the accretionary prism. **(b-c)** Simplified sketch showing the main sedimentary and tectonic events in the Mt. Massico area

(Modified after Smeraglia et a., 2019): **(b)** During late Tortonian-early Messinian times, orogenic compression generated a fault propagation anticline located in the northeastern part of the Mt. Massico ridge, juxtaposing pre-orogenic limestones in the hangingwall with syn-orogenic Tortonian sandstones in the footwall. **(c)** During late Messinian-early Pliocene times, out-of-sequence thrusting occurred and a ~3,300 m-thick stack of imbricate thrust sheets thrust onto the Tortonian-lower Messinian clastic deposits and calcarenites. At this stage the tectonic mélange develop at the base of the clastic deposits. Notice that remnants of such thrust sheets are located in the Mt. Petrino area (Fig. 2).

Figure 10. Simplified evolution of the Mt. Massico tectonic mélange (See Fig. 10b,c for the structural location of the evolution scheme). **(a)** During the early deformation stage, veins perpendicular to bedding develop within the clastic deposits in response to far field tectonic stress. **(b)** Initial shortening affect the clastic deposits generating a weak scaly foliation parallel respect to bedding (see Fig. 3a,b). **(c)** Progressive shortening generated S-C fabric and boudinage of competent bedding (limestones and sandstones). **(d)** During the late stage of deformation, the strongly deformed tectonic mélange develop. In particular, pervasive S-C tectonites develop within the weak (marls and shale) matrix and relicts of competent strata are deformed generating scattered clasts with sigmoidal shape. Notice that hemipelagic marls are scraped off and mixed within the tectonic mélange, while the underlying Meso-Cenozoic limestones are not deformed. The inset shows the different type of veins within the mélange (blocky and fibrous) and their structural position respect to stylolites.

Figure 11. Schematic evolutionary model for mélange-related veins evolution through time. Notice alternate cycles of mutually overprinting brittle (fracturing/veining) and ductile (pressure-solution and stylolites generation) processes.

Figure S1. (a) ^{40}Ar concentration versus age diagram. Notice that there is no correlation between ^{40}Ar concentration and ages of dated veins. **(b)** ^{4}He concentration versus age diagram. Notice that there is no correlation between ^{4}He concentration and ages of dated veins. **(c)** ^{3}He concentration versus age diagram. Notice that there is no correlation between ^{3}He concentration and ages of dated veins. **(d)** ^{3}He/^{4}He ratio (R/Ra) versus age diagram. Notice that there is no correlation between ^{3}He/^{4}He ratio (R/Ra) and ages of dated veins.

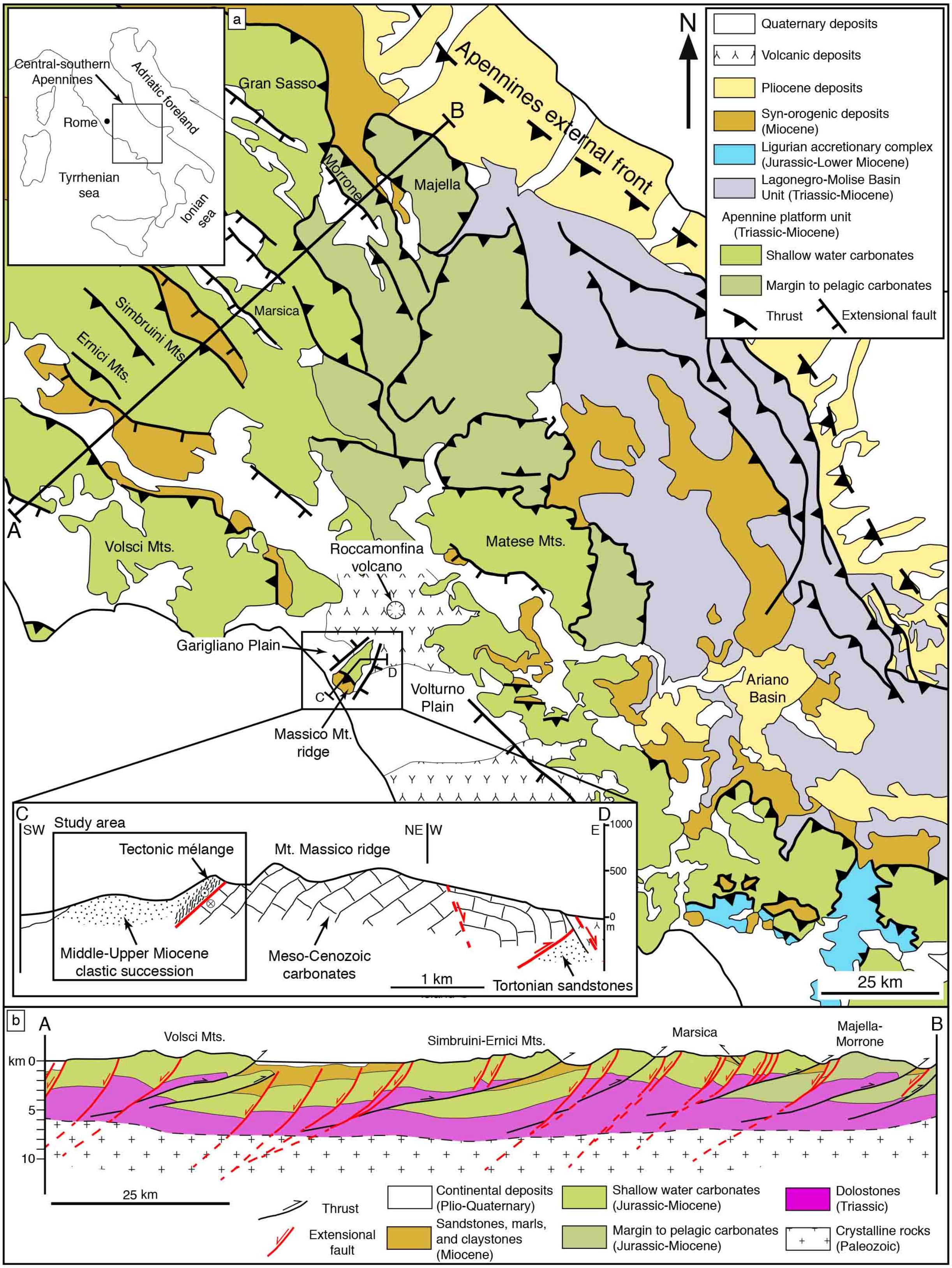

a
Central-southern Apennines
Adriatic foreland
Rome
Tyrrhenian sea
Ionian sea
Quaternary deposits
Volcanic deposits
Pliocene deposits
Syn-orogenic deposits (Miocene)
Ligurian accretionary complex (Jurassic-Lower Miocene)
Lagonegro-Molise Basin Unit (Triassic-Miocene)
Apennine platform unit (Triassic-Miocene)
Shallow water carbonates
Margin to pelagic carbonates
Thrust
Extensional fault
N
Apennines external front
Gran Sasso
Morrone
Majella
Marsica
Simbruini Mts.
Ernici Mts.
Volsci Mts.
Matese Mts.
Roccamonfina volcano
Garigliano Plain
Volturno Plain
Massico Mt. ridge
Ariano Basin
A
B
C
D
25 km
Study area
SW
NE W
E
Tectonic mélange
Mt. Massico ridge
Middle-Upper Miocene clastic succession
Meso-Cenozoic carbonates
Tortonian sandstones
1 km
1000
500
0
m
b
Volsci Mts.
Simbruini-Ernici Mts.
Marsica
Majella-Morrone
km 0
5
10
25 km
Thrust
Extensional fault
Continental deposits (Plio-Quaternary)
Sandstones, marls, and claystones (Miocene)
Shallow water carbonates (Jurassic-Miocene)
Margin to pelagic carbonates (Jurassic-Miocene)
Dolostones (Triassic)
Crystalline rocks (Paleozoic)

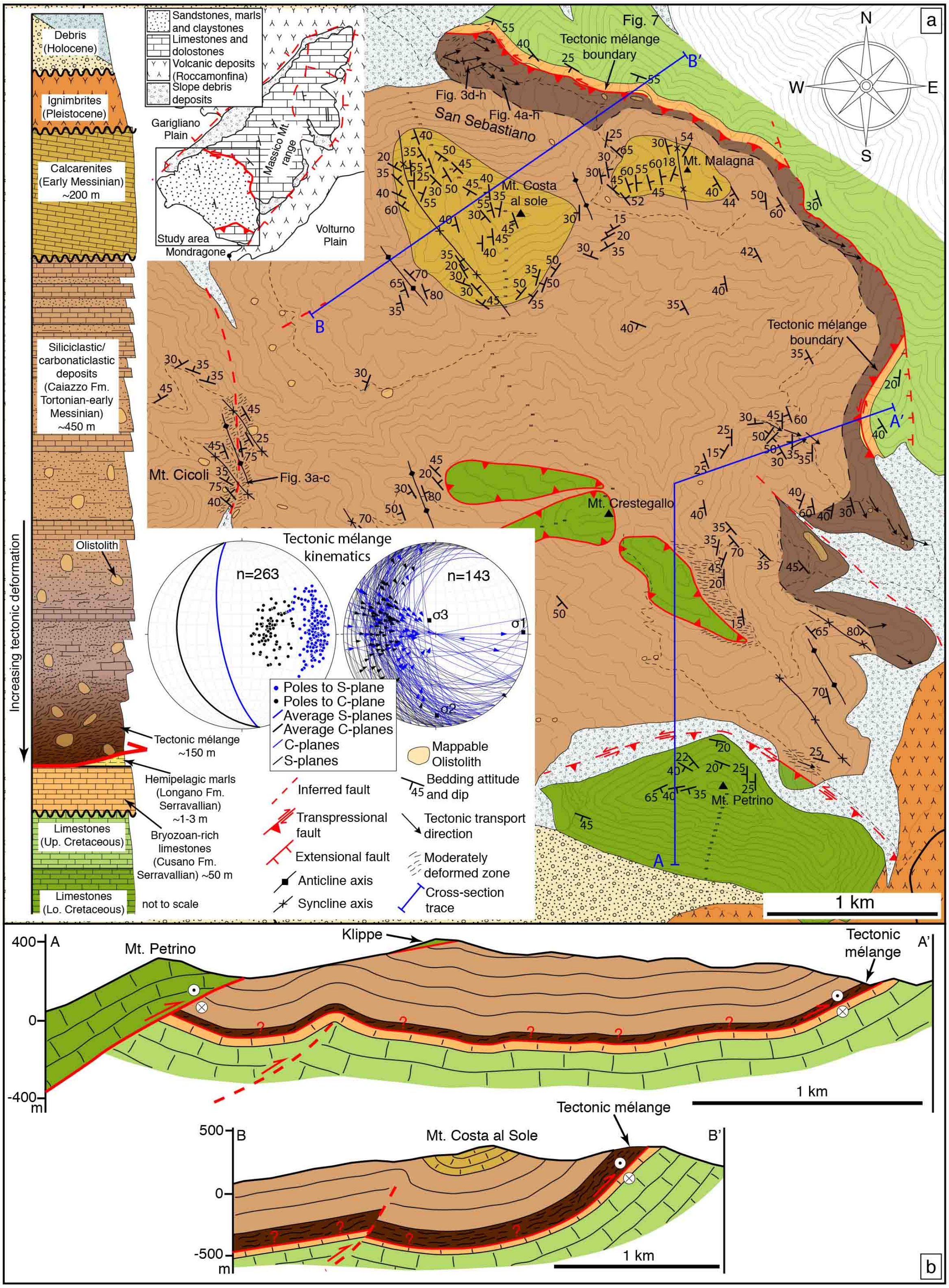

a
Fig. 7
Tectonic mélange boundary
San Sebastiano
Fig. 3d-h
Fig. 4a-h
Mt. Costa al sole
Mt. Malagna
Mt. Cicoli
Fig. 3a-c
Mt. Crestegallo
Mt. Petrino
Tectonic mélange boundary
Debris (Holocene)
Ignimbrites (Pleistocene)
Calcarenites (Early Messinian) ~200 m
Siliciclastic/ carbonaticlastic deposits (Caiazzo Fm. Tortonian-early Messinian) ~450 m
Olistolith
Increasing tectonic deformation
Tectonic mélange ~150 m
Hemipelagic marls (Longano Fm. Serravallian) ~1-3 m
Bryozoan-rich limestones (Cusano Fm. Serravallian) ~50 m
Limestones (Up. Cretaceous)
Limestones (Lo. Cretaceous)
not to scale
Sandstones, marls and claystones
Limestones and dolostones
Volcanic deposits (Roccamonfina)
Slope debris deposits
Garigliano Plain
Massico Mt. range
Study area
Mondragone
Volturno Plain
Tectonic mélange kinematics
n=263
n=143
σ3
σ1
σ2
Poles to S-plane
Poles to C-plane
Average S-planes
Average C-planes
C-planes
S-planes
Mappable Olistolith
Inferred fault
Bedding attitude and dip
Transpressional fault
Tectonic transport direction
Extensional fault
Moderately deformed zone
Anticline axis
Syncline axis
Cross-section trace
1 km
b
A
A'
Mt. Petrino
Klippe
Tectonic mélange
B
B'
Mt. Costa al Sole
Tectonic mélange
1 km

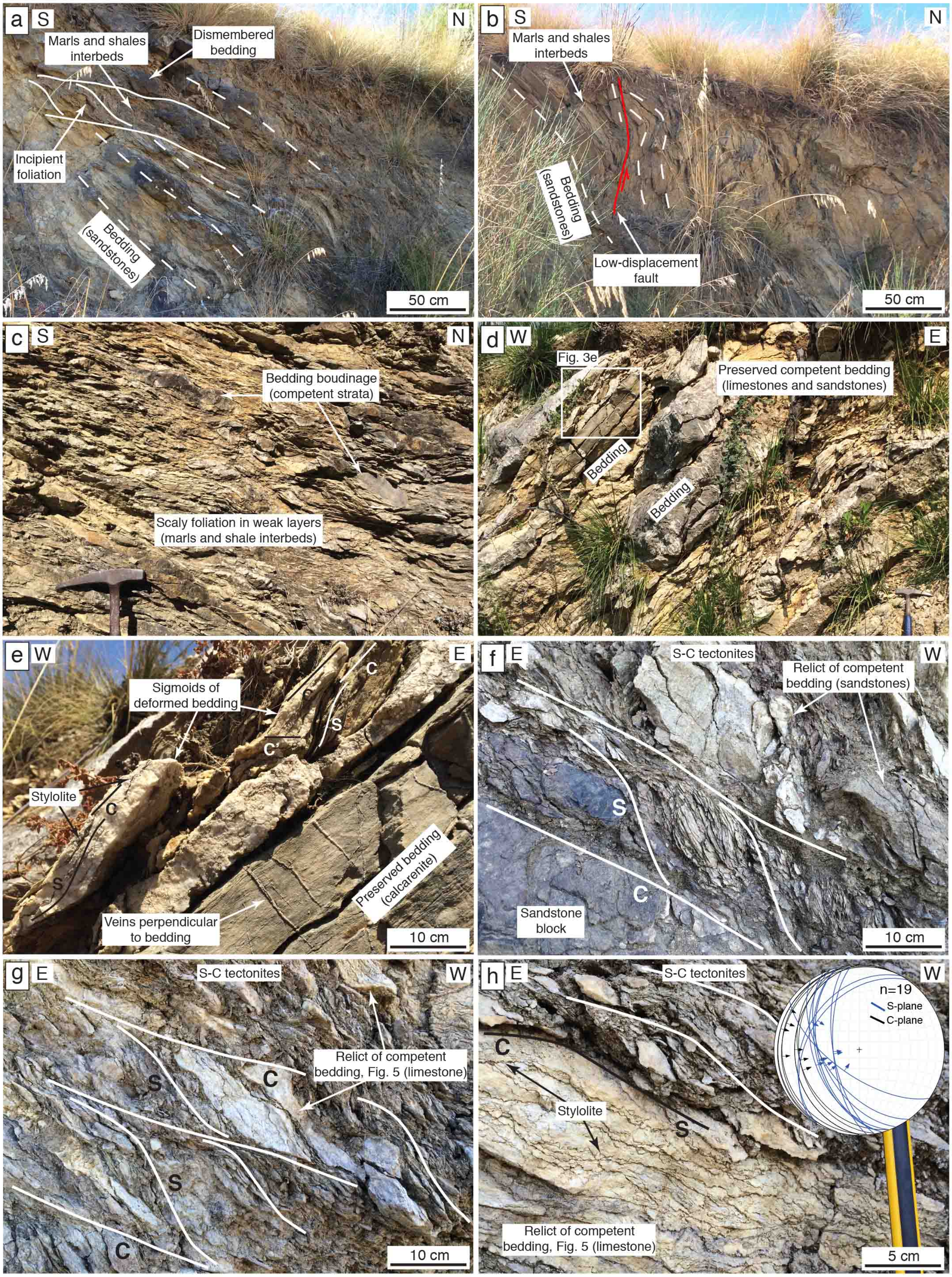

a
S
N
Marls and shales interbeds
Dismembered bedding
Incipient foliation
Bedding (sandstones)
50 cm
b
S
N
Marls and shales interbeds
Bedding (sandstones)
Low-displacement fault
50 cm
c
S
N
Bedding boudinage (competent strata)
Scaly foliation in weak layers (marls and shale interbeds)
d
W
E
Fig. 3e
Preserved competent bedding (limestones and sandstones)
Bedding
Bedding
e
W
E
Sigmoids of deformed bedding
Stylolite
C
S
C
C
S
Preserved bedding (calcarenite)
Veins perpendicular to bedding
10 cm
f
E
W
S-C tectonites
Relict of competent bedding (sandstones)
S
C
Sandstone block
10 cm
g
E
W
S-C tectonites
Relict of competent bedding, Fig. 5 (limestone)
S
C
S
C
10 cm
h
E
W
S-C tectonites
n=19
S-plane
C-plane
C
Stylolite
S
Relict of competent bedding, Fig. 5 (limestone)
5 cm

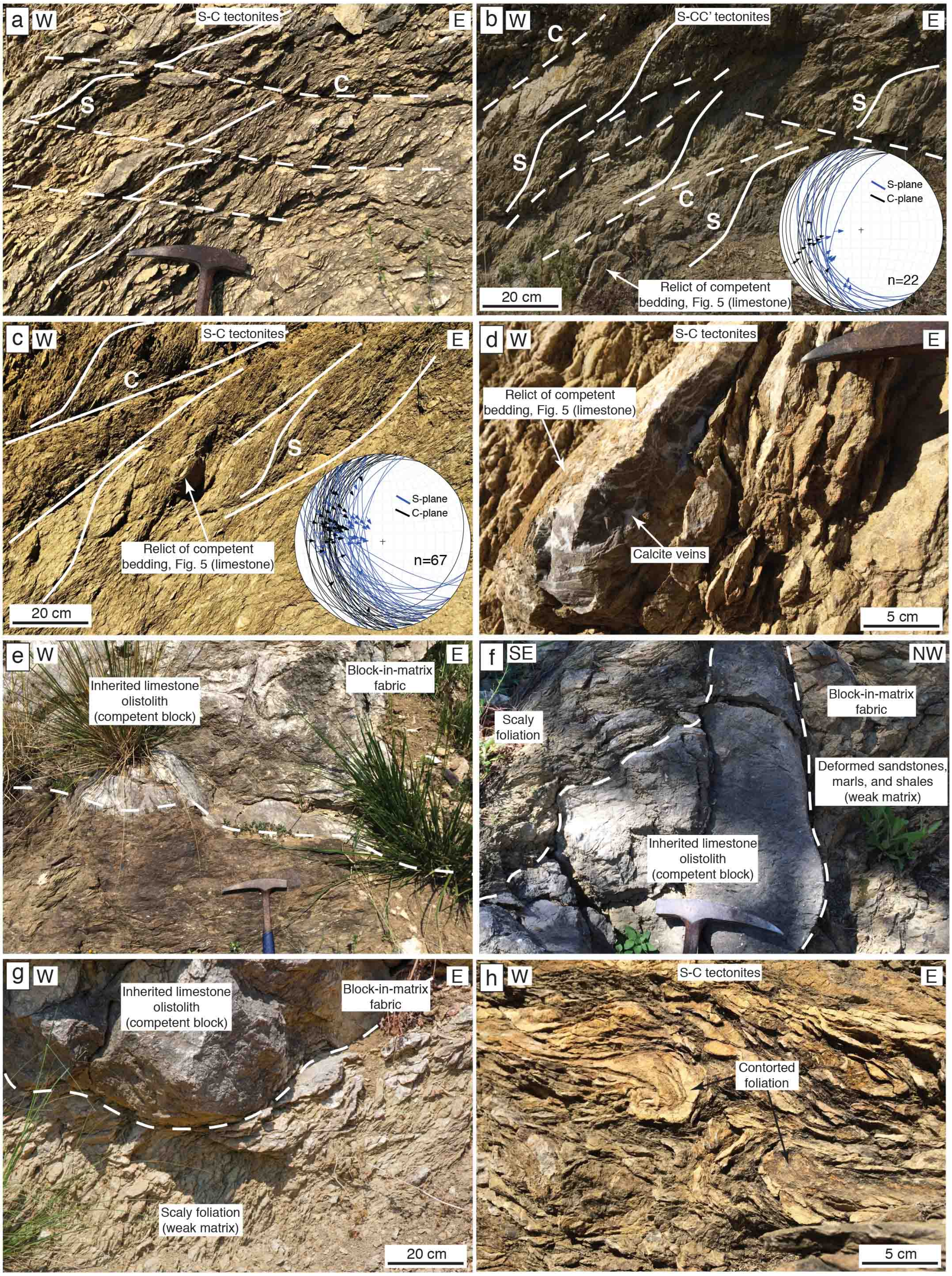

a
W
E
S-C tectonites
S
C
b
W
E
S-CC' tectonites
C
S
S
C
S
S-plane
C-plane
n=22
20 cm
Relict of competent bedding, Fig. 5 (limestone)
c
W
E
S-C tectonites
C
S
S-plane
C-plane
n=67
Relict of competent bedding, Fig. 5 (limestone)
20 cm
d
W
E
S-C tectonites
Relict of competent bedding, Fig. 5 (limestone)
Calcite veins
5 cm
e
W
E
Inherited limestone olistolith (competent block)
Block-in-matrix fabric
f
SE
NW
Scaly foliation
Block-in-matrix fabric
Deformed sandstones, marls, and shales (weak matrix)
Inherited limestone olistolith (competent block)
g
W
E
Inherited limestone olistolith (competent block)
Block-in-matrix fabric
Scaly foliation (weak matrix)
20 cm
h
W
E
S-C tectonites
Contorted foliation
5 cm

Relicts of competent bedding

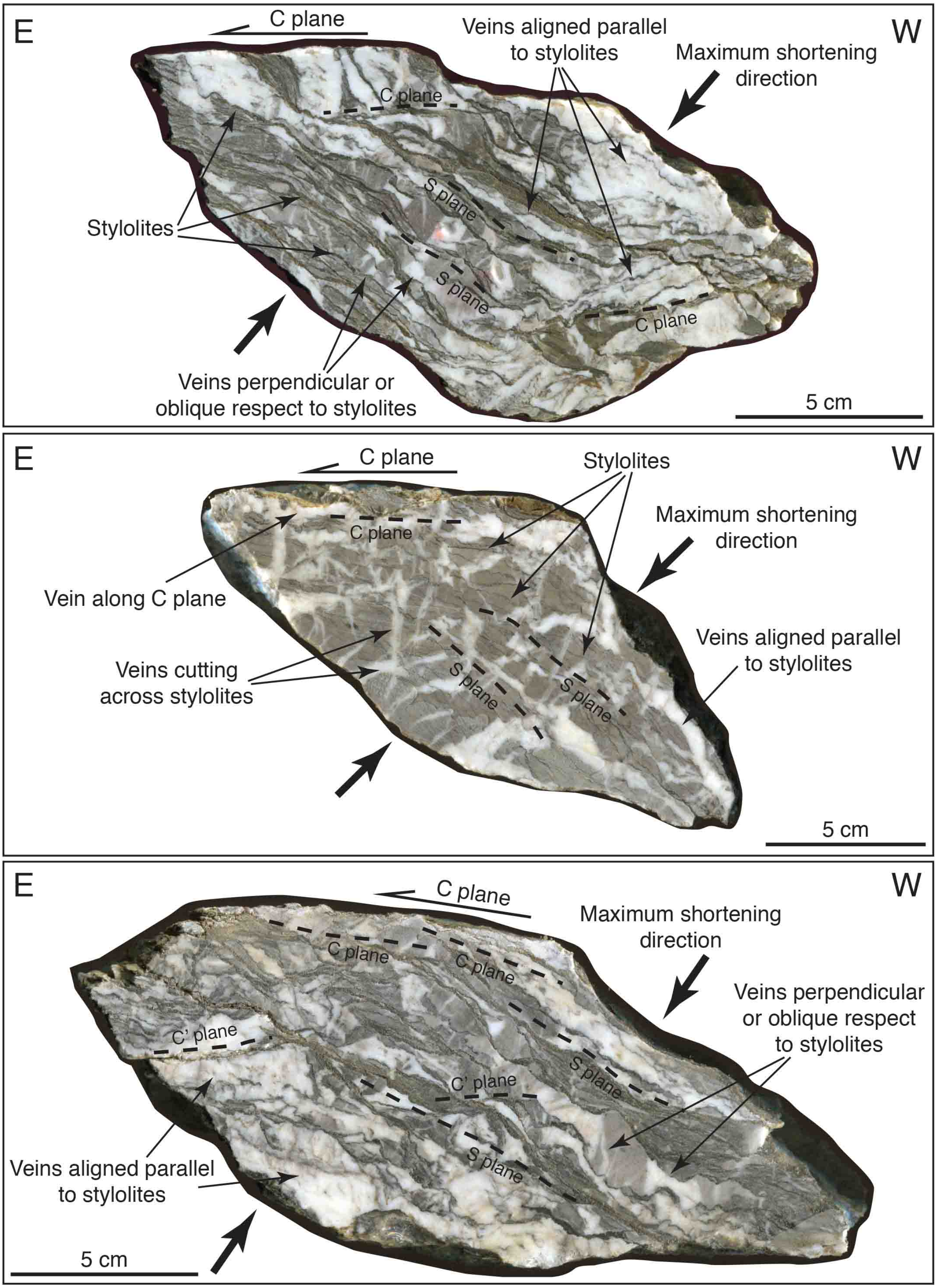

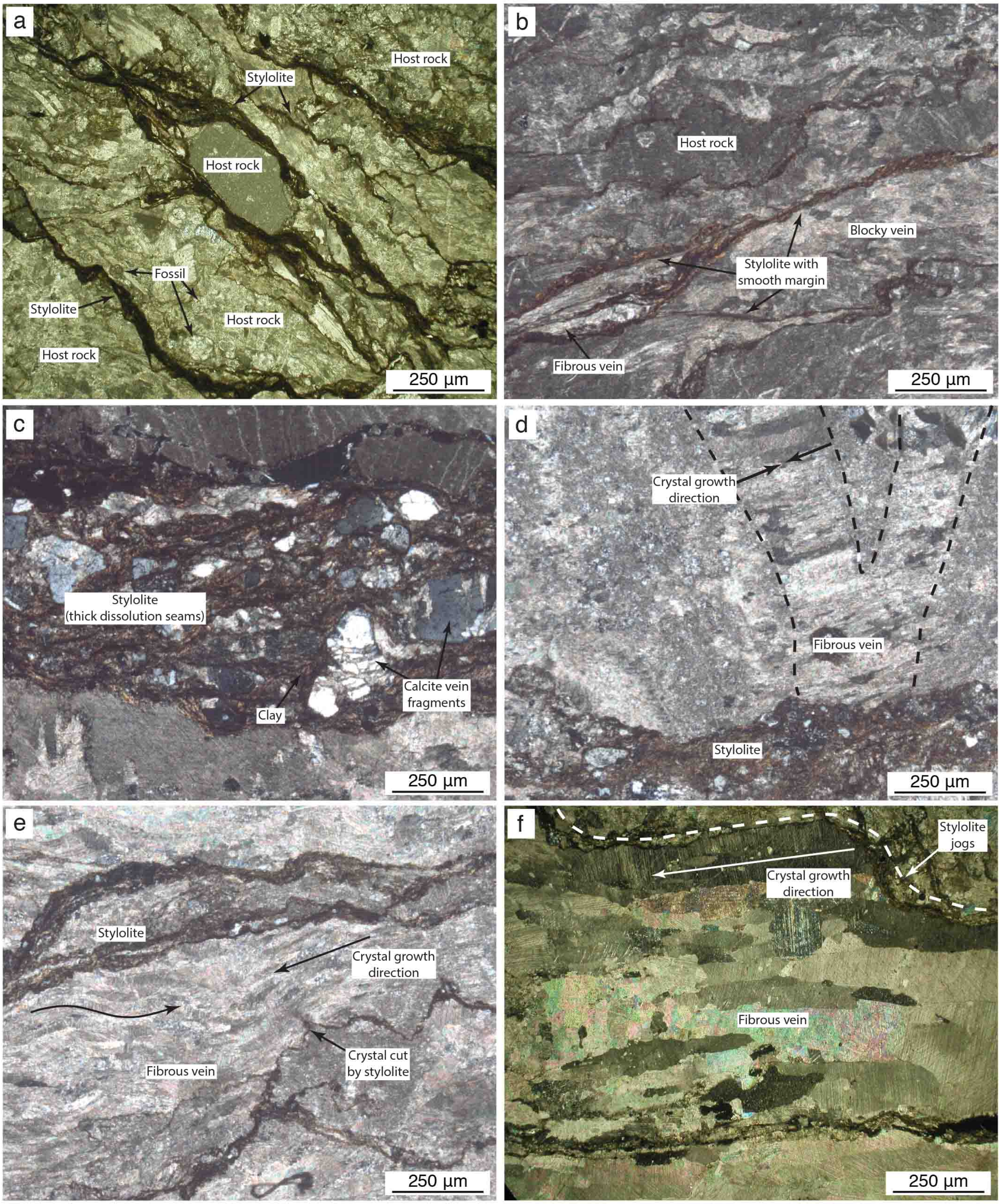

a
Host rock
Stylolite
Host rock
Fossil
Stylolite
Host rock
Host rock
250 µm
b
Host rock
Blocky vein
Stylolite with smooth margin
Fibrous vein
250 µm
c
Stylolite (thick dissolution seams)
Calcite vein fragments
Clay
250 µm
d
Crystal growth direction
Fibrous vein
Stylolite
250 µm
e
Stylolite
Crystal growth direction
Crystal cut by stylolite
Fibrous vein
250 µm
f
Stylolite jogs
Crystal growth direction
Fibrous vein
250 µm

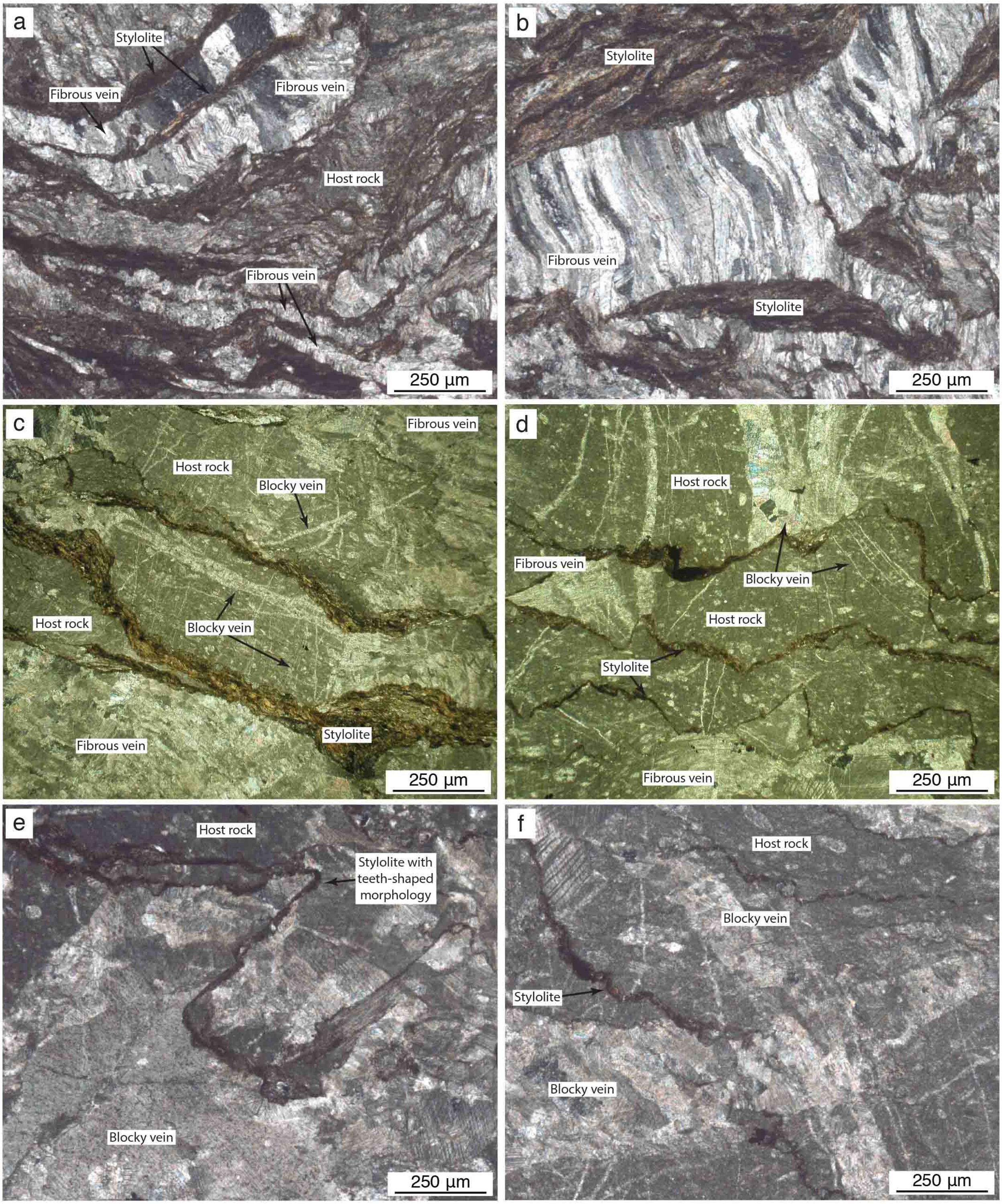
a
Stylolite
Fibrous vein
Fibrous vein
Host rock
Fibrous vein
250 µm
b
Stylolite
Fibrous vein
Stylolite
250 µm
c
Fibrous vein
Host rock
Blocky vein
Host rock
Blocky vein
Stylolite
Fibrous vein
250 µm
d
Host rock
Fibrous vein
Blocky vein
Host rock
Stylolite
Fibrous vein
250 µm
e
Host rock
Stylolite with teeth-shaped morphology
Blocky vein
250 µm
f
Host rock
Blocky vein
Stylolite
Blocky vein
250 µm

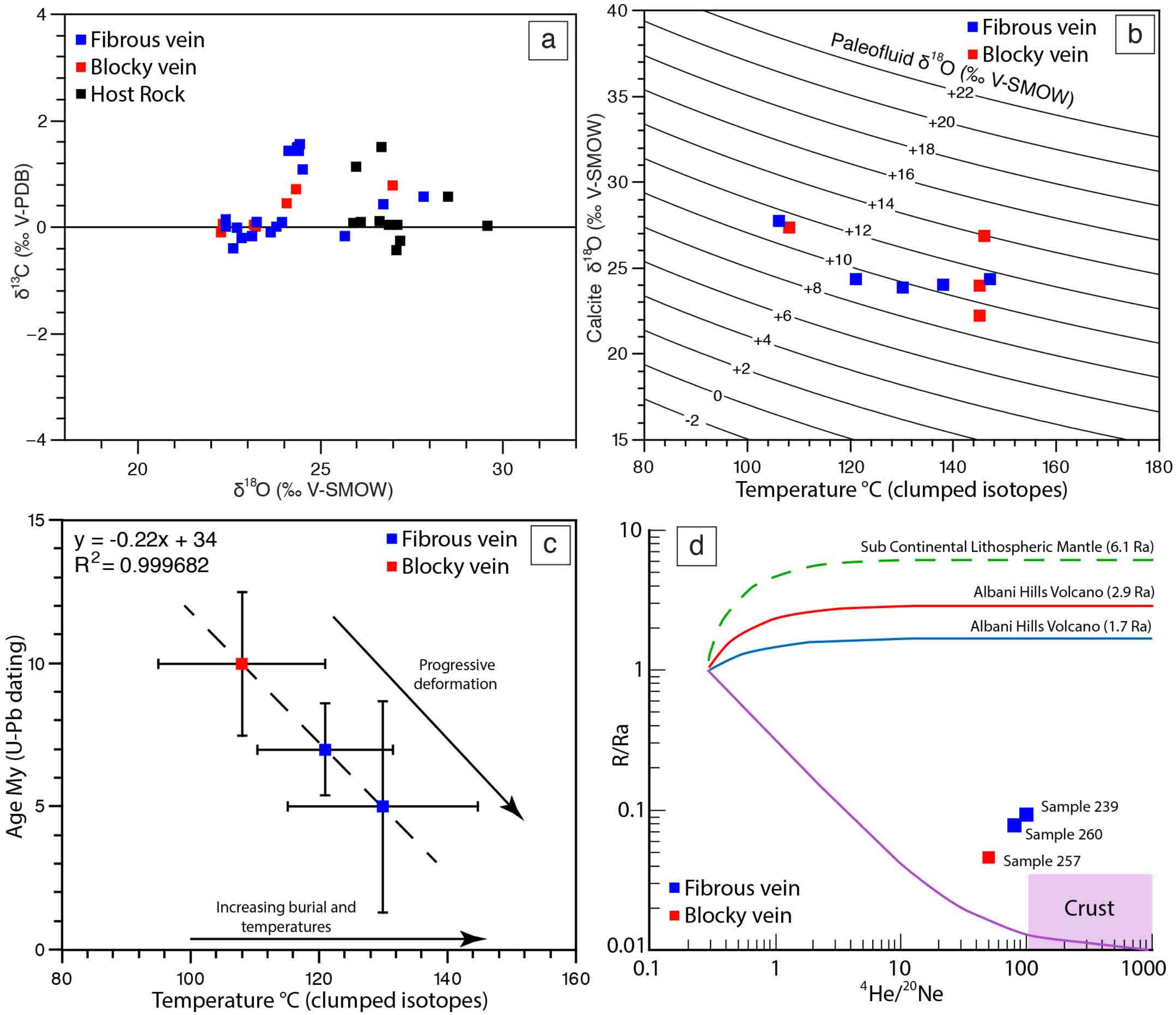

a
Fibrous vein
Blocky vein
Host Rock
δ13C (‰ V-PDB)
δ18O (‰ V-SMOW)
b
Fibrous vein
Blocky vein
Paleofluid δ18O (‰ V-SMOW)
+22
+20
+18
+16
+14
+12
+10
+8
+6
+4
+2
0
-2
Calcite δ18O (‰ V-SMOW)
Temperature °C (clumped isotopes)
c
y = -0.22x + 34
R2= 0.999682
Fibrous vein
Blocky vein
Progressive deformation
Increasing burial and temperatures
Age My (U-Pb dating)
Temperature °C (clumped isotopes)
d
Sub Continental Lithospheric Mantle (6.1 Ra)
Albani Hills Volcano (2.9 Ra)
Albani Hills Volcano (1.7 Ra)
Sample 239
Sample 260
Sample 257
Crust
Fibrous vein
Blocky vein
R/Ra
4He/20Ne

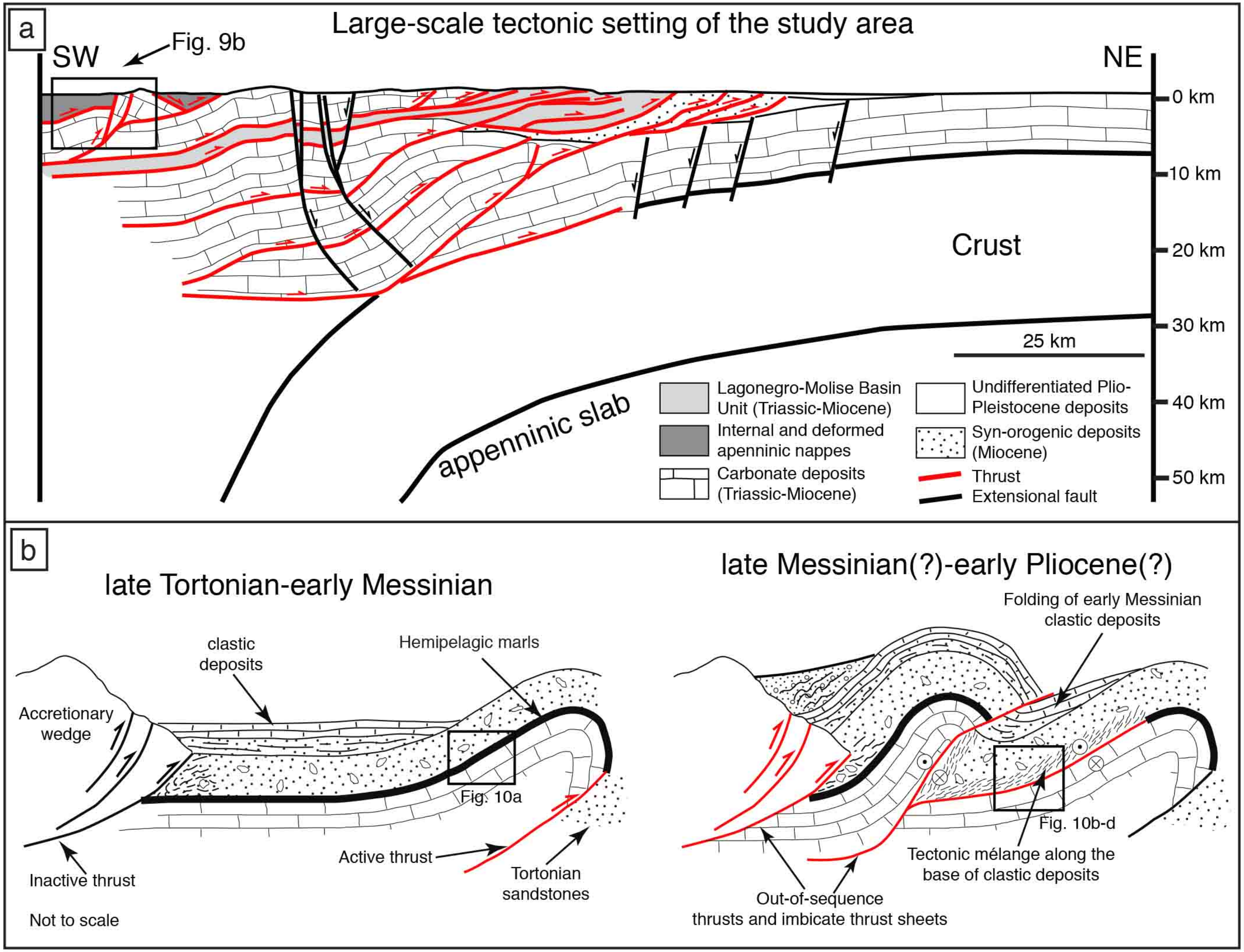
a
Large-scale tectonic setting of the study area
SW
Fig. 9b
NE
0 km
10 km
20 km
30 km
40 km
50 km
Crust
25 km
appenninic slab
Lagonegro-Molise Basin Unit (Triassic-Miocene)
Internal and deformed apenninic nappes
Carbonate deposits (Triassic-Miocene)
Undifferentiated Plio-Pleistocene deposits
Syn-orogenic deposits (Miocene)
Thrust
Extensional fault
b
late Tortonian-early Messinian
clastic deposits
Hemipelagic marls
Accretionary wedge
Fig. 10a
Inactive thrust
Active thrust
Tortonian sandstones
Not to scale
late Messinian(?)-early Pliocene(?)
Folding of early Messinian clastic deposits
Fig. 10b-d
Tectonic mélange along the base of clastic deposits
Out-of-sequence thrusts and imbicate thrust sheets

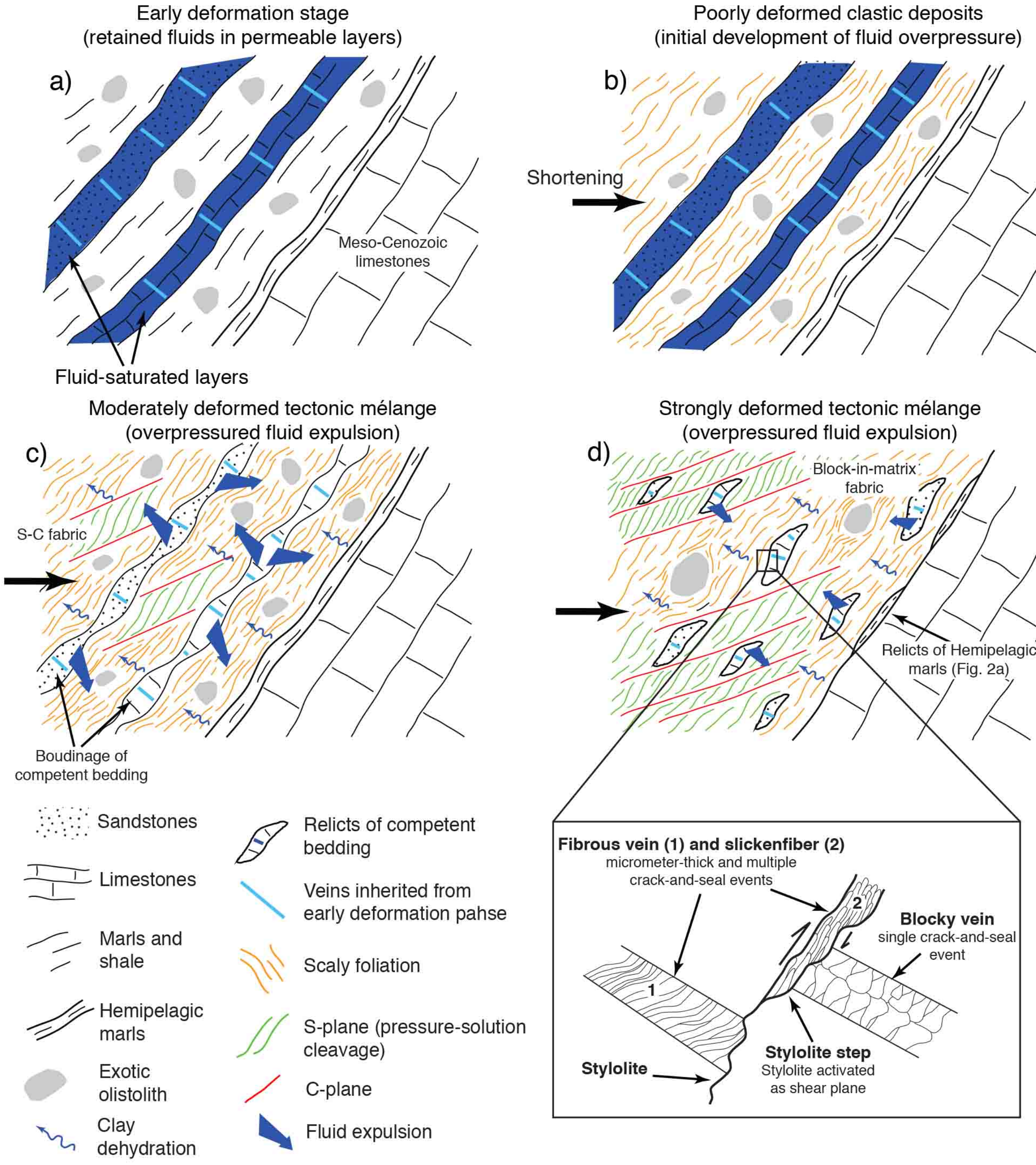
Early deformation stage
(retained fluids in permeable layers)
a)
Meso-Cenozoic limestones
Fluid-saturated layers
Poorly deformed clastic deposits
(initial development of fluid overpressure)
b)
Shortening
Moderately deformed tectonic mélange
(overpressured fluid expulsion)
c)
S-C fabric
Boudinage of competent bedding
Strongly deformed tectonic mélange
(overpressured fluid expulsion)
d)
Block-in-matrix fabric
Relicts of Hemipelagic marls (Fig. 2a)
Sandstones
Limestones
Marls and shale
Hemipelagic marls
Exotic olistolith
Clay dehydration
Relicts of competent bedding
Veins inherited from early deformation pahse
Scaly foliation
S-plane (pressure-solution cleavage)
C-plane
Fluid expulsion
Fibrous vein (1) and slickenfiber (2)
micrometer-thick and multiple crack-and-seal events
1
2
Blocky vein
single crack-and-seal event
Stylolite
Stylolite step
Stylolite activated as shear plane

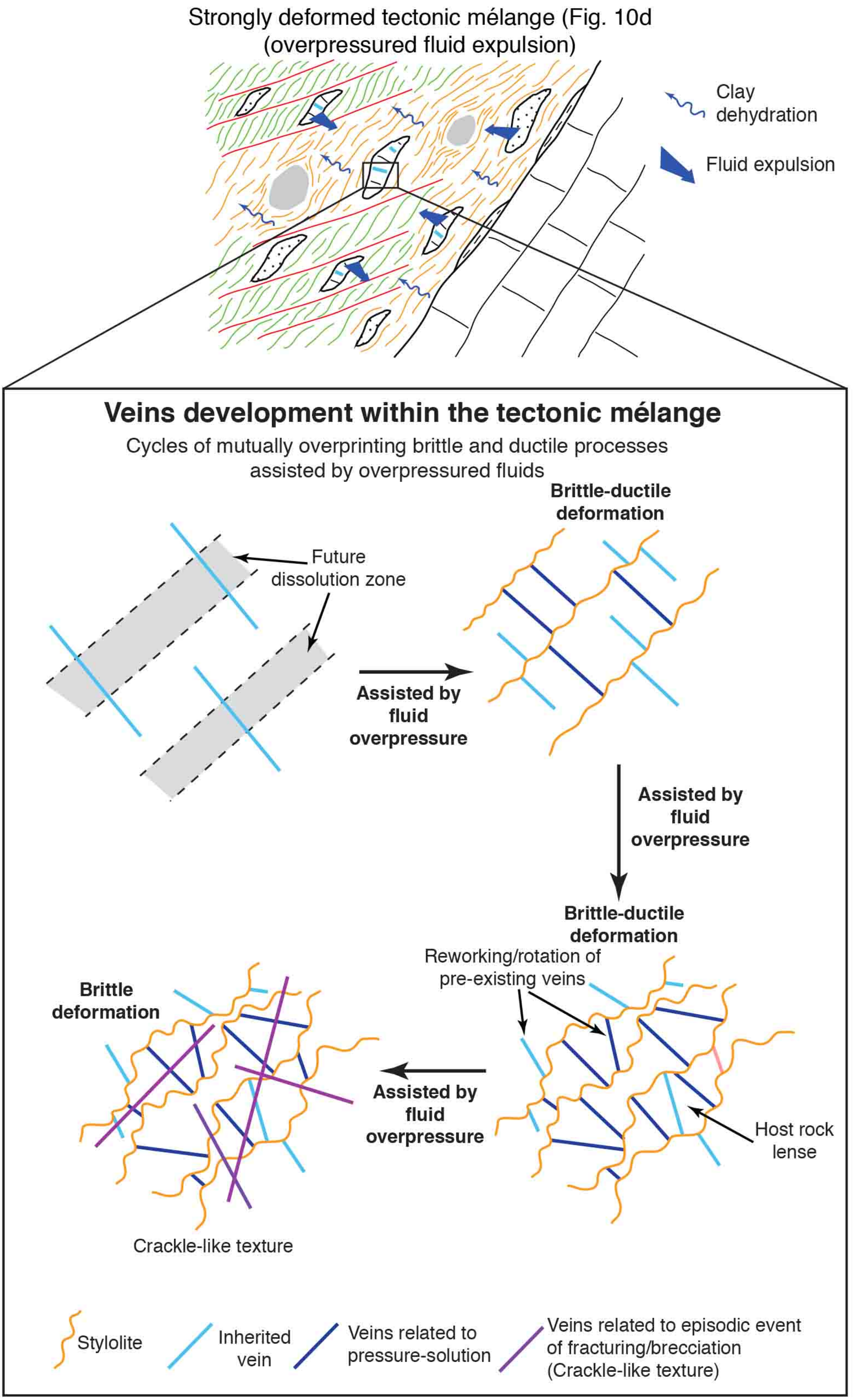

Strongly deformed tectonic mélange (Fig. 10d
(overpressured fluid expulsion)
Clay
dehydration
Fluid expulsion
Veins development within the tectonic mélange
Cycles of mutually overprinting brittle and ductile processes
assisted by overpressured fluids
Future
dissolution zone
Assisted by
fluid
overpressure
Brittle-ductile
deformation
Assisted by
fluid
overpressure
Brittle-ductile
deformation
Reworking/rotation of
pre-existing veins
Host rock
lense
Assisted by
fluid
overpressure
Brittle
deformation
Crackle-like texture
Stylolite
Inherited
vein
Veins related to
pressure-solution
Veins related to episodic event
of fracturing/brecciation
(Crackle-like texture)

Declaration of interests

The authors declare that they have no known competing financial interests or personal relationships that could have appeared to influence the work reported in this paper.

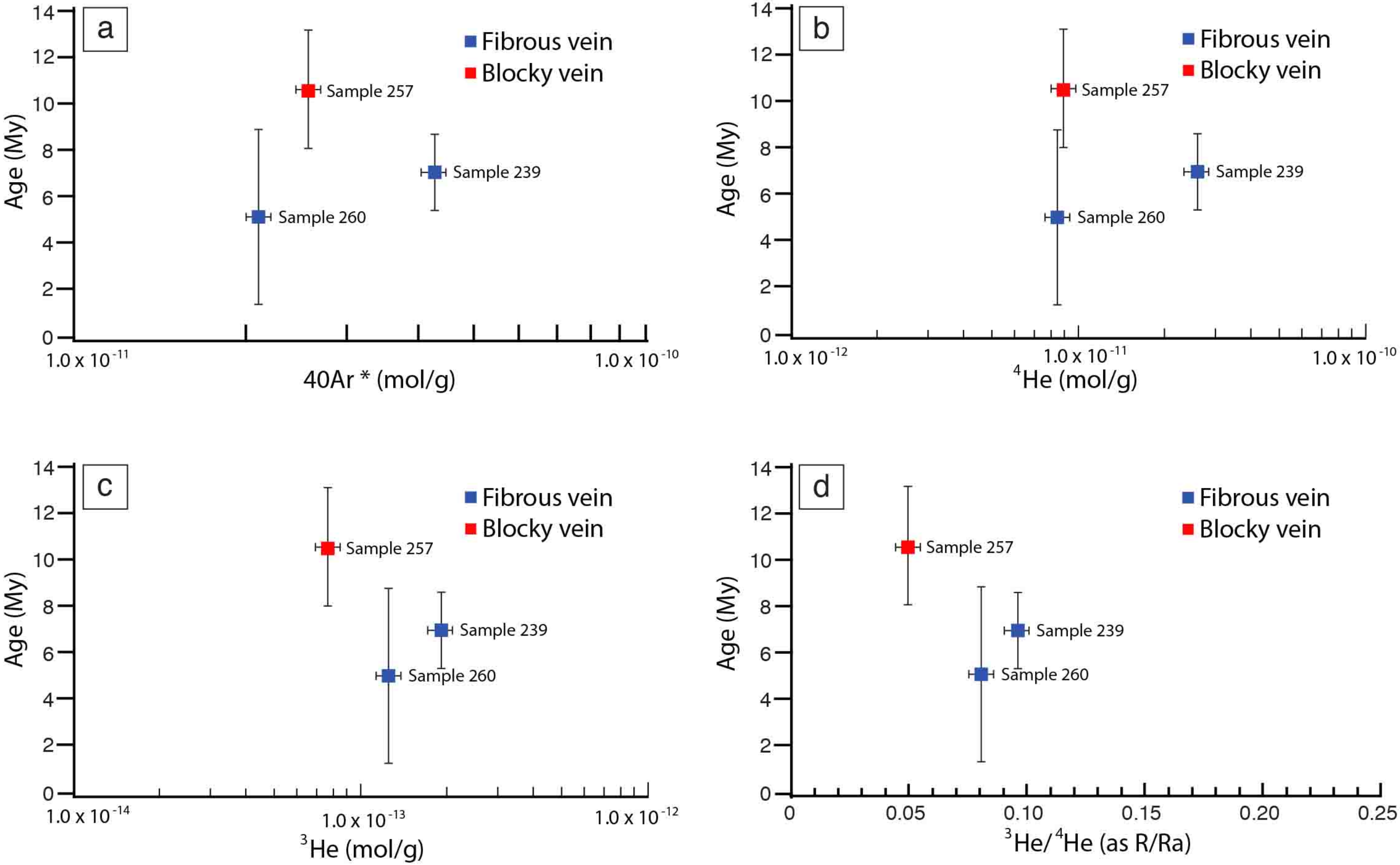

a
Fibrous vein
Blocky vein
Sample 257
Sample 239
Sample 260
Age (My)
40Ar * (mol/g)
1.0 x 10^-11
1.0 x 10^-10
b
Fibrous vein
Blocky vein
Sample 257
Sample 239
Sample 260
Age (My)
4He (mol/g)
1.0 x 10^-12
1.0 x 10^-11
1.0 x 10^-10
c
Fibrous vein
Blocky vein
Sample 257
Sample 239
Sample 260
Age (My)
3He (mol/g)
1.0 x 10^-14
1.0 x 10^-13
1.0 x 10^-12
d
Fibrous vein
Blocky vein
Sample 257
Sample 239
Sample 260
Age (My)
3He/4He (as R/Ra)

Locality	Number	Sample type	δ^{13}C ‰ (V-PDB)	δ^{18}O ‰ (V-SMOW)
N 41°09’59’’ E 13°53’03’’	242	Blocky vein	0.45	24.05
N 41°09’59’’ E 13°53’03’’	234	Blocky vein	0.73	24.31
N 41°09’59’’ E 13°53’03’’	233-2	Blocky vein	0.80	26.97
N 41°09’59’’ E 13°53’03’’	238-1	Fibrous vein	-0.38	22.61
N 41°09’59’’ E 13°53’03’’	259	Fibrous vein	0.59	27.82
N 41°09’59’’ E 13°53’03’’	235	Fibrous vein	0.44	26.70
N 41°09’59’’ E 13°53’03’’	237-1	Fibrous vein	1.09	24.51
N 41°09’59’’ E 13°53’03’’	237-2	Fibrous vein	1.56	24.42
N 41°09’59’’ E 13°53’03’’	237-3	Fibrous vein	1.45	24.40
N 41°09’59’’ E 13°53’03’’	237-4	Fibrous vein	1.50	24.35
N 41°09’59’’ E 13°53’03’’	254-1	Fibrous vein	-0.09	23.62
N 41°09’59’’ E 13°53’03’’	254-2	Fibrous vein	-0.16	25.65
N 41°09’59’’ E 13°53’03’’	254-3	Fibrous vein	-0.19	22.84
N 41°09’59’’ E 13°53’03’’	260-2	Fibrous vein	0.11	23.24
N 41°09’59’’ E 13°53’03’’	260-3	Blocky vein	0.06	23.17
N 41°09’59’’ E 13°53’03’’	260-4	Blocky vein	0.01	23.22
N 41°09’59’’ E 13°53’03’’	260-5	Fibrous vein	0.11	23.94
N 41°09’59’’ E 13°53’03’’	260-8	Fibrous vein	0.02	23.79
N 41°09’59’’ E 13°53’03’’	265	Fibrous vein	0.16	22.40
N 41°09’59’’ E 13°53’03’’	265-2	Fibrous vein	0.00	22.69
N 41°09’59’’ E 13°53’03’’	265-3	Fibrous vein	0.01	22.40
N 41°09’59’’ E 13°53’03’’	265-5	Blocky vein	-0.08	22.27
N 41°09’59’’ E 13°53’03’’	265-6	Blocky vein	0.01	22.35
N 41°09’59’’ E 13°53’03’’	265-7	Blocky vein	0.07	22.31
N 41°09’59’’ E 13°53’03’’	266	Fibrous vein	1.44	24.11
N 41°09’59’’ E 13°53’03’’	266 bis	Fibrous vein	-0.16	23.10
N 41°09’59’’ E 13°53’03’’	266 S-plane	Fibrous vein	1.52	24.38
N 41°09’59’’ E 13°53’03’’	HR 1	Host rock	0.58	28.48
N 41°09’59’’ E 13°53’03’’	HR 2	Host rock	1.15	25.97
N 41°09’59’’ E 13°53’03’’	HR 3	Host rock	0.04	29.56
N 41°09’59’’ E 13°53’03’’	HR 4	Host rock	-0.42	27.06
N 41°09’59’’ E 13°53’03’’	HR 5	Host rock	0.13	26.60
N 41°09’59’’ E 13°53’03’’	HR 6	Host rock	0.05	27.10
N 41°09’59’’ E 13°53’03’’	HR 7	Host rock	0.06	26.85
N 41°09’59’’ E 13°53’03’’	HR 8	Host rock	0.09	25.89
N 41°09’59’’ E 13°53’03’’	HR 9	Host rock	1.52	26.65
N 41°09’59’’ E 13°53’03’’	HR 10	Host rock	-0.24	27.16
N 41°09’59’’ E 13°53’03’’	HR 11	Host rock	0.11	26.08

Table S1. Summary of δ^{18}O- and δ^{13}C-isotopes analyses on mélange-related mineralizations

Sample type	Replicates	$\delta^{13}C$ V-PDB	$\delta^{13}C$ V-PDB SD	$\delta^{18}O$ V-PDB	$\delta^{18}O$ V-PDB SD	$\delta^{18}O$ V-SMOW	Δ47 CDES	Δ47 CDES SD	Δ47 CDES SE	Average T °C	SD	SE	68% Conf Level	95% Conf Level	$\delta^{18}O$ paleofluid (VSMOW) (O'Neil et al.. 1969)
Blocky vein	10	0.78	0.01	-3.89	0.02	26.91	0.424	0.027	0.009	146	21.6	6.8	7.2	15.4	13.7
Blocky vein	11	0.44	0.02	-6.73	0.04	23.98	0.426	0.026	0.008	145	23.9	7.2	7.6	16.1	10.8
Blocky vein	8	0.67	0.02	-3.41	0.04	27.41	0.477	0.027	0.009	108	15.5	5.5	5.9	13.0	10.9
Blocky vein	13	0.02	0.11	-8.38	0.24	22.28	0.426	0.027	0.007	145	21.5	6.0	6.2	13.0	9.1
Fibrous vein	7	1.57	0.02	-6.32	0.03	24.41	0.424	0.026	0.010	147	22.3	8.4	9.1	20.6	11.3
Fibrous vein	10	0.06	0.02	-6.32	0.03	24.40	0.457	0.023	0.007	121	14.7	4.6	4.9	10.5	9.1
Fibrous vein	11	0.59	0.03	-3.04	0.06	27.79	0.482	0.034	0.010	106	20.4	6.2	6.4	13.7	11.0
Fibrous vein	8	0.10	0.01	-6.83	0.03	23.88	0.449	0.025	0.008	130	17.7	6.2	6.7	14.8	9.4
Fibrous vein	10	1.53	0.01	-6.64	0.02	24.08	0.433	0.015	0.005	138	11.0	3.5	3.7	7.9	10.3

Table S2. Summary of clumped isotopes analyses. SD, Standard Deviation; SE, Standard Error; CDES

Sample	Weight (g)	^{4}He mol/g	^{4}He err	^{3}He mol/g	^{3}He err	^{20}Ne mol/g	^{20}Ne err	H_2O+CO_2 mol/g	N_2 mol/g	^{40}Ar mol/g	^{40}Ar err	^{40}Ar* mol/g	^{40}Ar* err	He/Ar	N_2/Ar	He/Ne	He/Ar*	Err	R/Ra	Rc/Ra	Err tot +/-	^{40}Ar/^{36}Ar	Error (%)
239	0,185	$2,59 \times 10^{-11}$	0,02	$3,38 \times 10^{-18}$	4,60	$2,68 \times 10^{-13}$	0,65	$8,28 \times 10^{-6}$	$6,67 \times 10^{-7}$	$1,84 \times 10^{-10}$	0,04	$4,26 \times 10^{-11}$	0,08	$1,41 \times 10^{-1}$	3633,289	96,5	0,61	0,1	0,10	0,09	0,004	388,88	0,07
260	0,112	$8,42 \times 10^{-11}$	0,01	$9,23 \times 10^{-19}$	5,76	$1,06 \times 10^{-13}$	0,69	$1,12 \times 10^{-6}$	$3,07 \times 10^{-7}$	$8,99 \times 10^{-11}$	0,07	$2,10 \times 10^{-11}$	0,16	$9,37 \times 10^{-2}$	3413,257	79,4	0,40	0,2	0,08	0,08	0,005	389,94	0,15
257	0,118	$8,91 \times 10^{-11}$	0,01	$6,04 \times 10^{-19}$	6,11	$1,73 \times 10^{-13}$	0,61	$2,58 \times 10^{-6}$	$4,25 \times 10^{-7}$	$1,38 \times 10^{-10}$	0,06	$2,57 \times 10^{-11}$	0,13	$6,48 \times 10^{-2}$	3092,841	51,7	0,35	0,1	0,05	0,05	0,003	367,29	0,12

Table S3. Summary of isotope data from fluid inclusions analysis of sin-tectonic calcite veins from the tectonic mélange

grain		207Pba (cps)	U (ppb)	Pb (ppb)	Th/U	206Pbd/238U	±2s (%)	207Pbd/206Pb	±2s (%)
A06	257	471600	1813	2050	1,45	0,6812	3,0	0,8316	0,29
A07		743113	2742	3190	1,59	0,6995	2,3	0,8354	0,26
A08		260035	1484	1140	1,75	0,4622	3,8	0,8341	0,36
A09		285988	1597	1222	1,33	0,461	3,8	0,8312	0,32
A10		337476	1242	1442	1,83	0,6985	3,7	0,833	0,31
A11		859984	2505	3710	1,34	0,8915	3,0	0,8333	0,26
A12		848268	2668	3655	1,04	0,825	2,4	0,8325	0,28
A13		848529	2950	3677	1,28	0,7508	2,8	0,8314	0,25
A14		178565	743	770	1,83	0,623	2,6	0,836	0,41
A15		289446	1019	1254	1,31	0,7413	2,9	0,8326	0,33
A16		600706	3321	2920	1,48	0,5291	12,8	0,8341	0,33
A17		39317	28	170	0,90	3,589	3,2	0,8401	0,83
A18		49523	41	216	0,27	3,142	4,4	0,8369	0,9
A19		26662	26	115	0,70	2,711	2,9	0,8369	1
A357	239	12788	285	65	0,02	0,1384	2,4	0,8223	1,2
A358		18181	191	96	0,02	0,303	2,8	0,8235	0,99
A359		14325	241	75	0,01	0,1893	2,6	0,8241	1,4
A360		10828	280	57	0,01	0,1228	2,4	0,8226	1,2
A361		10706	363	57	0,00	0,09543	2,5	0,8109	1,2
A362		10988	348	58	0,01	0,1019	2,9	0,8148	1,5
A363		12475	330	65	0,00	0,1201	2,2	0,8217	1,2
A364		17402	368	92	0,01	0,1525	2,6	0,8174	1,2
A365		15176	390	80	0,01	0,1241	2,2	0,824	1,4
A366		6761	174	36	0,04	0,1245	2,3	0,821	1,4
A367		8980	177	47	0,04	0,1606	2,6	0,8241	1,5
A368		4920	426	27	0,02	0,03843	2,7	0,8025	1,9
A369		4639	372	24	0,02	0,04009	2,9	0,8108	1,5
A370		5947	327	32	0,01	0,05904	2,5	0,8161	1,6
A371		9201	336	49	0,01	0,08899	2,3	0,8169	1,1
A372		9057	447	48	0,01	0,06531	2,2	0,8188	1,5
A373		6908	380	37	0,01	0,05856	2,6	0,8195	1,6
A374		7199	428	38	0,00	0,05435	2,4	0,8226	1,4
A375		5955	393	32	0,02	0,04907	2,7	0,813	1,5
A376		6757	314	36	0,02	0,06952	2,5	0,8158	1,7
A377		7776	396	42	0,01	0,06384	2,6	0,8122	1,6
A378		27871	67	148	0,09	1,339	2,3	0,8237	0,82
A379		36109	87	191	0,14	1,332	2,5	0,8282	0,66
A380		29563	77	157	0,08	1,237	2,5	0,827	0,79
A381		29869	62	155	0,08	1,511	2,2	0,8303	0,65
A382		6778	270	37	0,02	0,08265	2,7	0,816	1,4
A388		5744	357	31	0,02	0,05281	3,1	0,8086	1,7

A389		8213	359	44	0,01	0,07527	3,4	0,8178	1,3
A390		4465	466	24	0,00	0,03182	2,5	0,7943	1,6
A391		7002	296	38	0,00	0,07781	3,1	0,8133	1,9
A392		4777	310	26	0,01	0,05026	3,2	0,819	1,7
A393		4529	355	25	0,01	0,04272	2,6	0,8027	2,3
A394		5007	525	28	0,00	0,03264	2,6	0,7964	1,6
A395		6174	372	34	0,00	0,05504	2,5	0,8121	1,6
A396		6364	386	35	0,00	0,0553	2,4	0,8108	1,6
A397		7127	430	39	0,00	0,05461	2,3	0,8224	1,1
A398		6037	407	33	0,00	0,04976	2,6	0,8068	1,5
A279	260	13497	219	67	0,33	0,1848	5,4	0,8327	1,3
A280		5001	160	26	0,41	0,09853	3,6	0,8033	1,8
A281		5932	277	30	0,28	0,06634	4,0	0,8151	1,9
A282		4217	185	21	0,24	0,07005	3,4	0,8215	3
A288		2222	143	12	0,16	0,04938	4,1	0,7978	2,9
A289		2093	100	10	0,11	0,0627	3,5	0,8231	3
A290		4225	138	21	0,20	0,09378	3,8	0,8269	2,2
A291		2031	115	11	0,08	0,05615	3,3	0,8012	3,1
A292		3437	183	18	0,24	0,05916	2,6	0,8036	2,7
A293		2266	189	12	0,03	0,03706	3,3	0,8226	2,8
A294		2120	141	11	0,04	0,04753	4,1	0,8059	2,3
A295		2135	197	11	0,02	0,03456	2,8	0,7943	2,6
A296		3288	182	17	0,08	0,05596	4,8	0,8266	2,2
A297		1759	175	9	0,02	0,03171	3,6	0,8073	3,1
A298		1526	188	8	0,01	0,0265	3,3	0,7891	3,4
A299		1516	207	8	0,01	0,0253	3,2	0,7562	2,5
A300		2051	221	11	0,01	0,02958	4,8	0,7964	2,5
A301		3149	190	16	0,04	0,05305	3,5	0,7994	2,8
A302		3162	58	16	0,07	0,1711	2,6	0,8152	2,7
A303		5499	57	28	0,09	0,2944	2,9	0,8301	1,8
A304		1879	225	10	0,01	0,02713	3,2	0,7866	3,1
A305		2075	244	11	0,01	0,02725	3,9	0,7959	2,9
A306		3289	226	17	0,04	0,0464	4,5	0,8082	3,1
A307		1723	248	9	0,01	0,02306	3,2	0,7729	3,4
A308		2257	190	12	0,02	0,03743	3,2	0,813	3,2
A309		3923	20	20	1,77	0,602	3,9	0,8285	1,9
A310		3197	132	17	0,06	0,0771	4,4	0,809	2,7

Table S4. Summary of in situ U, Pb, and Th analyses of syn-tectonic calcite veins from the tectonic Mélange

Methods

Stable and Clumped isotopes

The stable and clumped isotope composition of the carbonates were determined at ETH Zürich using a Thermo Fisher Scientific MAT253 mass spectrometer coupled to a Kiel IV carbonate preparation device, following the method described in Schmid and Bernasconi (2010), Meckler et al. (2014), and Müller et al. (2017). The Kiel IV device included a PoraPakQ trap kept at -40°C to eliminate potential organic contaminants. Prior to each sample run, the pressure-dependent backgrounds were determined on all beams to correct for non-linearity effects in the mass spectrometer according to Bernasconi et al. (2013). During each run of the autosampler of 46 positions, 3 replicates each of 95-110 µg of different samples and 5 replicates the carbonate standards ETH-1, ETH-2, and 10 replicates of the standard ETH-3 were analyzed with the LIDI method (Müller et al. 2017). The samples were measured over a period of three weeks to avoid biases due to short-term variations in the performance of the instruments. All calculations and corrections were done with the software Easotope (John and Bowen, 2016) using the revised IUPAC parameters for ^{17}O correction as suggested by Daeron et al. (2016). Temperatures were calculated using the O'Neal et al. (1969) calibration recalculated using fully recalculated values of the ETH standards and of calibration samples as described in Bernasconi et al. (2018). The complete results are reported in Table S3 in relation to the carbon dioxide equilibrium scale (CDES) projected to an acid digestion temperature of 25°C.

Analytical technique for fluid inclusions

We determined the H_2O+CO_2, and N_2 content and the elemental and isotope composition of noble gases (He, Ne, and Ar) in fluid inclusions of Sample 239, Sample 257, and Sample 260 of calcite veins from Mt. Massico tectonic mélange. Samples were prepared and analyzed in the laboratories of Istituto Nazionale di Geofisica e Vulcanologia (INGV), Sezione di Palermo (Italy), following the preparation and analytical protocols described in Smeraglia et al. (2018) and Rizzo et al. (2019). Complete results are reported in Figs. 8d, S2 and Table S3.

H_2O+CO_2 in fluid inclusions have been extracted and quantified in a stainless steel crusher during noble gas extraction, which gives a good indication of the moles of gaseous matrix of fluid inclusions but does not completely preserve these species from adsorption and fractionation in powders and stainless steel. In the first stage, part of the vein samples has been gently broken, sieved with a diameter >1 mm mesh. The selected crystals were cleaned in an ultrasonic bath. The portion of the selected sample material was weighed in an analytical balance, thus loaded into a stainless-steel crusher baked for 48-72h at 120°C in order to put in ultra-high-vacuum conditions (10^{-9} mbar). Fluid inclusions were released by a single-step (in-vacuum) crushing performed at 200 bar. The amount of material loaded for each analysis was ~0.1-0.2 g. This procedure is the most conservative in order to minimize the contribution of cosmogenic ^3He and radiogenic ^4He possibly grown/trapped in the crystal lattice (e.g., Hilton et al., 1993, 2002). The atmospheric component was separated and quantified at the time of crushing by observing the following steps: immediately after crushing, we read the total gas pressure ($N_2+O_2+H_2O+CO_2$+noble gases). Then, N_2+O_2+noble gases were separated from the H_2O+CO_2 by using a "cold finger" immersed in liquid nitrogen (T= -196 ° C) that allows freezing H_2O and CO_2. After this step, we checked again the total pressure for quantifying the atmospheric component. Noble gases separated from H_2O and CO_2 were further cleaned in an ultra-high vacuum (10^{-9} - 10^{-10} mbar) purification line, and all the species of the gas mixture, except noble gases, were removed from four getters.

Helium (^3He and ^4He) and neon (^{20}Ne, ^{21}Ne and ^{22}Ne) isotopes were measured separately by two different split-flight-tube mass spectrometers (Helix SFT-Thermo). The values of the $^3He/^4He$ ratio are expressed as R/Ra (where Ra is the $^3He/^4He$ ratio of air, which is equal to 1.39×10^{-6}). In addition, due to the presence of air He contamination, the R/Ra values were corrected based on the measured $^4He/^{20}Ne$ ratio (e.g., Sano et al., 1985) and are expressed as Rc/Ra values. However, the corrected ratios show minimum to negligible differences respect to raw $^{3}He/^{4}He$ ratios. The analytical uncertainty of He isotopic ratio is ≤ 6%, while that of $^{20}Ne/^{22}Ne$ is <0.17%.

Argon isotopes (^{36}Ar, ^{38}Ar and ^{40}Ar) were analyzed by a multicollector mass spectrometer (GVI Argus), with an analytical uncertainty < 0.14%. The uncertainty in the determinations of He, Ne, and Ar elemental contents was less than 0.1%. Typical blanks for He, Ne and Ar were $<10^{-15}$, $<10^{-15}$ and $<10^{-14}$ mol, respectively, and are at least two orders of magnitude lower than analytical signals of samples. Further details about the sample preparation and analytical procedures are available in Rizzo et al. (2018, 2019) and Smeraglia et al. (2018).

References

Bernasconi S.M., Müller I. A., Bergmann K.D., Breitenbach S. F. M., Fernandez, A., Hodell D. A., Jaggi M., Meckler A.N. Millan I., and Ziegler M. (2018) Reducing uncertainties in carbonate clumped isotope analysis through consistent carbonate-based standardization. *Geochemistry Geophysics Geosystems* 19. https://doi.org/10.1029/2017GC007385

Bernasconi, S.M., Hu, B., Wacker, U., Fiebig, J., Breitenbach, S.F.M., Rutz, T., 2013. Background effects on Faraday collectors in gas-source mass spectrometry and implications for clumped isotope measurements. *Rapid Communications in Mass Spectrometry,* 27, 603–612. doi:10.1002/rcm.6490

Breitenbach S.F.M, Mlenek-Vautravers, M.J., Grauel A.L., Bernasconi S.M. Müller, I.A., Rolfe, J. Gázquez F., Greaves M. Elderfield, H. and Hodell, D.A. (in revision) Coupled Mg/Ca and clumped isotope analyses of foraminifera provide consistent water temperatures. Geochimica Cosmochimica Acta.

Dennis, K.J., Affek, H.P., Passey, B.H., Schrag, D.P., Eiler, J.M., 2011. Defining an absolute reference frame for "clumped" isotope studies of CO_2. Geochimimica et Cosmochimica Acta, 75, 7117–7131. doi:10.1016/j.gca.2011.09.025.

Hilton, D.R., Fischer, T.P., Marty, B., 2002. Noble gases and volatile recycling at subduction zones. Rev. Min. and Geoch. 47, 319-370. https://doi.org/10.2138/rmg.2002.47.9.

Hilton, D.R., Hammerschmidt, K., Teufel, S., Friedrichsen, H. 1993. Helium isotope characteristics of Andean geothermal fluids and lavas. Earth Planet. Sci. Lett. 120, 265-282. https://doi.org/10.1016/0012-821X(93)90244-4.

John, C.M., Bowen, D., 2016. Community software for challenging isotope analysis: First applications of “Easotope” to clumped isotopes. *Rapid Communications in Mass Spectrometry,* 30, 2285–2300. doi:10.1002/rcm.7720

Kele, S., Breitenbach, S. F., Capezzuoli, E., Meckler, A. N., Ziegler, M., Millan, I. M., Kluge, T., Deak, J., Hanselmann, K., John, C.M., Yan, H., Liu, Z., Bernasconi, S.M. (2015). Temperature dependence of oxygen-and clumped isotope fractionation in carbonates: A study of travertines and tufas in the 6–95 °C temperature range. Geochimica et Cosmochimica Acta 168, 172-192. https://doi.org/10.1016/j.gca.2015.06.032.

Meckler, A.N., Ziegler, M., Millán, M.I., Breitenbach, S.F.M., Bernasconi, S.M., 2014. Long-term performance of the Kiel carbonate device with a new correction scheme for clumped isotope measurements. Rapid Comm. in Mass Spectrom. 28, 1705-1715.

Müller, I.A., Fernandez, A., Radke, J., Dijk, J. Van, Bowen, D., Schwieters, J., Bernasconi, S.M., 2017. Carbonate clumped isotope analyses with the long-integration dual-inlet (LIDI) workflow : scratching at the lower sample weight boundaries. *Rapid Communications in Mass ,* 2, 1057–1066. doi:10.1002/rcm.7878

O'Neil, J. R., Clayton, R. N., & Mayeda, T. K. (1969). Oxygen isotope fractionation in divalent metal carbonates. *The Journal of Chemical Physics*, *51*(12), 5547-5558.

Rizzo AL, Pelorosso B, Coltorti M, Ntaflos T, Bonadiman C, Matusiak-Małek M, Italiano F and Bergonzoni G (2018) Geochemistry of Noble Gases and CO_2 in Fluid Inclusions From Lithospheric Mantle Beneath Wilcza Góra (Lower Silesia, Southwest Poland). Front. Earth Sci. 6:215. doi: 10.3389/feart.2018.00215

Rizzo, A. L., Uysal, I. T., Mutlu, H., Ünal-İmer, E., Dirik, K., Yüce, G., et al. (2019). Geochemistry of fluid inclusions in travertines from western and northern Turkey: Inferences on the role of active faults in fluids circulation. Geochemistry, Geophysics, Geosystems, 20. https://doi.org/10.1029/2019GC008453

Sano, Y., Urabe, A., Wakita, H., Chiba, H., Sakai, H., 1985. Chemical and isotopic compositions of gases in geothermal fluids in Iceland. Geoch. J. 19, 135-148. https://doi.org/10.2343/geochemj.19.135.

Schmid, T.W., Bernasconi, S.M., 2010. An automated method for "clumped-isotope" measurements on small carbonate samples. *Rapid Communications in Mass Spectrometry* , 24, 1955–1963. doi:10.1002/rcm.4598.